Journal of Cluster Science (2026) 37:98
https://doi.org/10.1007/s10876-026-03053-8

ORIGINAL PAPER

Sustainable Design of LrGO–Ag–Au–Cu_xO Hybrid Nanocomposites with Superior Catalytic and Photocatalytic Efficiency in Aqueous Pollutant Degradation

Bengü Getiren Sevinç[1,2] · Salih Açıl[1] · Furkan Soysal[3] · Zafer Çıplak[4] · Atila Yıldız[5] · Nuray Yıldız[1]

Received: 8 January 2026 / Accepted: 5 June 2026
© The Author(s) 2026

Abstract

Cetraria islandica (L.) Ach. lichen extract was employed as a bioinorganic reducing and stabilizing agent for the single-step green synthesis of a quaternary LrGO-Ag-Au-Cu_xO nanocomposite integrating lichen-reduced graphene oxide (LrGO), silver (Ag), gold (Au), and copper oxide (Cu_xO). XRD Rietveld refinement confirmed the coexistence of four crystalline phases – Ag (56.9 wt%), Au (28.9 wt%), CuO (7.5 wt%), and Cu_2O (6.7 wt%) – Alongside the LrGO matrix, while XPS established the zero-valent states of Ag and Au and the formation of CuO/Cu_2O heterojunctions. TEM analysis revealed a narrow nanoparticle size distribution with an average of 6.03 ± 2.61 nm, and BET analysis yielded a specific surface area of 11 $m^2\ g^{-1}$. The dual functionality of the nanocomposite was evaluated through two model reactions. In the catalytic reduction of 4-nitrophenol (4-NP) to 4-aminophenol (4-AP) using $NaBH_4$, the LrGO-Ag-Au-Cu_xO (1:1:1) nanocomposite exhibited an apparent rate constant of 0.0078 ± 0.0003 s^{-1} at a catalyst loading of 0.172 mg mL^{-1}, maintaining stable activity over 11 consecutive cycles. Under visible LED irradiation, the nanocomposite achieved a methylene blue (MB) degradation efficiency of 97.67 ± 1.15% within 180 min, with a rate constant of 0.0219 ± 0.00265 min^{-1}. Radical trapping experiments identified •OH and $•O_2^-$ as the dominant reactive species. These results establish *Cetraria islandica* extract as an effective green synthesis medium for the fabrication of multifunctional quaternary nanocomposites with competitive dual catalytic and photocatalytic performance.

Keywords Green synthesis · Nanocomposites · Catalytic performance · Photocatalytic degradation

Introduction

Water pollution caused by industrial effluents poses growing challenges for water treatment systems worldwide. Among the toxic contaminants discharged into aquatic systems, organic dyes and nitroaromatic compounds are particularly difficult to remove through standard treatment processes due to their chemical stability and toxicity. Methylene blue (MB), a cationic thiazine dye used in textile, pharmaceutical, and biological industries, has been associated with skin irritation, respiratory problems, and mutagenic effects at elevated concentrations. Similarly, 4-nitrophenol (4-NP), listed as a priority pollutant by the United States Environmental Protection Agency, is generated as a byproduct in the manufacture of pesticides, pharmaceuticals, and explosives, and is toxic to aquatic organisms even at trace concentrations [1, 2]. These characteristics have prompted research into more effective and sustainable degradation methods.

✉ Nuray Yıldız
nyildiz@eng.ankara.edu.tr

1 Department of Chemical Engineering, Faculty of Engineering, Ankara University, Ankara 06100, Türkiye

2 Power Electronics, Faculty of Electrical Engineering, Mathematics & Computer Science (EEMCS), University of Twente, Enschede 7522 NB, The Netherlands

3 Department of Chemical Engineering, Faculty of Engineering and Natural Sciences, Ankara Yıldırım Beyazıt University, Ankara 06010, Türkiye

4 Department of Chemical Engineering, Faculty of Engineering, Sivas Cumhuriyet University, Sivas 58140, Türkiye

5 Department of Biology, Faculty of Science, Ankara University, Ankara 06100, Türkiye

Published online: 19 June 2026

Among the various approaches investigated for pollutant remediation, heterogeneous catalysis and semiconductor-based photocatalysis have been widely investigated due to their ability to degrade organic contaminants under mild conditions [3]. Copper oxides (CuO and Cu_2O) are two p-type semiconductors that have attracted attention as photocatalytic materials. CuO has a monoclinic crystal structure with a narrow band gap of 1.6 eV, excellent solar light absorption, and high chemical stability. Cu_2O, one of the earliest identified semiconductors, has a cubic structure and a direct band gap ranging from 2.0 to 2.2 eV, making both materials responsive to visible light irradiation [4, 5]. However, the reported band gap values of copper oxides are known to vary considerably depending on the synthesis method, morphology, phase composition, and measurement technique [6, 7]. Both oxides are naturally abundant, low in toxicity, and cost-effective, which makes them attractive for catalytic and photocatalytic applications. The formation of CuO/Cu_2O heterojunctions improves charge separation and reduces electron-hole recombination compared to single-phase systems, which is a key limitation in semiconductor photocatalysis [5, 8]. Reduced graphene oxide (rGO), with its high electron mobility and chemical stability, functions as an effective support for metal oxide nanoparticles, improving interfacial charge transfer and extending light absorption of the resulting nanocomposites [3, 8].

The incorporation of plasmonic noble metal nanoparticles, particularly silver (Ag) and gold (Au), into semiconductor-based photocatalytic systems has been shown to improve their catalytic and photocatalytic performance. Ag and Au nanoparticles display localized surface plasmon resonance (LSPR), which arises from the collective oscillation of free electrons under visible light irradiation [9–11]. This plasmonic excitation enhances light harvesting, generates hot electrons that can be injected into the conduction band of adjacent semiconductors, and intensifies the local electromagnetic field, contributing to increased generation of reactive oxygen species [9]. The interaction between Ag and Au nanoparticles and CuO/Cu_2O heterojunctions has been reported to broaden visible light absorption and facilitate charge separation at the metal-semiconductor interface, improving the catalytic and photocatalytic activity of the composite system [8, 12].

Alongside compositional design, the synthesis route influences the structural, morphological, and functional properties of nanocomposite materials. Conventional chemical synthesis methods typically rely on hazardous reducing agents, high temperatures, and toxic solvents, which limits their broader applicability. Green synthesis approaches utilizing plant and lichen extracts offer a more environmentally friendly alternative, typically operating under mild conditions and avoiding hazardous reagents [12–15]. The phytochemical constituents of these extracts, including polyphenols, polysaccharides, and secondary metabolites, act as reducing agents for metal ions and as capping agents that control nanoparticle growth and prevent aggregation. Lichen extracts have received comparatively little attention as reducing agents in nanoparticle synthesis despite their rich phytochemical content. *Cetraria islandica* (L.) Ach., a fruticose lichen containing usnic acid, lichenin, and various phenolic compounds, has previously been used in the green synthesis of Ag and Au nanoparticles and rGO-based nanocomposites with controlled morphology and functional properties [14, 17].

The present study reports the green synthesis of a quaternary lichen-reduced graphene oxide (LrGO)-Ag-Au-Cu_xO (CuO/Cu_2O) nanocomposite using *Cetraria islandica* (L.) Ach. extract as the reducing and stabilizing agent. The extract simultaneously facilitated the reduction of graphene oxide (GO) to LrGO and the formation of Ag, Au, and Cu_xO (CuO/Cu_2O) nanoparticles on the LrGO surface in a single-step process. The resulting nanocomposite combines the plasmonic properties of Ag and Au nanoparticles, the heterojunction photocatalytic activity of CuO/Cu_2O, and the electron transport capability of the LrGO matrix. The dual functionality of the nanocomposite was evaluated through its catalytic performance in the reduction of 4-NP in the presence of $NaBH_4$ and its photocatalytic activity in the degradation of MB under visible LED light irradiation. To the best of our knowledge, the use of *Cetraria islandica* extract for the synthesis of a quaternary LrGO–Ag–Au–Cu_xO nanocomposite with dual catalytic and photocatalytic application has not been previously reported, which distinguishes this work from previously reported systems [3, 8, 12].

Materials and Methods

Materials

C. islandica (L.) Ach. was collected from Çankırı, Turkey. Graphite oxide was obtained from Grafen Chemical Industries (Turkey). Chloroauric acid trihydrate ($HAuCl_4.3H_2O$) was purchased (PubChem CID: 44134746), along with silver nitrate ($AgNO_3$, ≥ 99.5%, Sigma Aldrich) and copper (II) sulfate pentahydrate ($CuSO_4 \cdot 5H_2O$, for analysis EMSURE® ACS, ISO, Reag. Ph Eur, Merck). Additional reagents included sodium hydroxide (NaOH, reagent grade≥98%, Sigma), methylene blue (MB, for Reag. Ph Eur, Merck), 4-Nitrophenol (4-NP, reagent grade≥98% for synthesis, Merck), and sodium borohydride ($NaBH_4$, fine granular for synthesis, Merck).

Synthesis of LrGO–Ag–Au–Cu_xO Nanocomposite

The inorganic–organic hybrid LrGO–Ag–Au–Cu_xO nanocomposite was synthesized via a green bioinorganic method using *Cetraria islandica* (L.) Ach. extract, with the lichen preparation procedure provided in the Supplementary Material. Figure S1 illustrates the synthesis process of the LrGO–Ag–Au–Cu_xO nanocomposite. First, 25 mg of graphite oxide was exfoliated in 50 mL of deionized (DI) water and sonicated in an ultrasonic bath for 60 min to obtain a homogeneous GO dispersion. Subsequently, 20 mM aqueous solutions of inorganic metal precursors—$AgNO_3$, $HAuCl_4$, and $CuSO_4$—were added dropwise to the GO dispersion at different molar ratios ($AgNO_3$:$HAuCl_4$:$CuSO_4$; 0.25:0.25:1, 0.5:0.5:1, 1:1:1, 1:1:2, and 1:1:4), followed by sonication for 1 h. The volume of each precursor solution was adjusted according to the target molar ratio, with the total reaction volume kept constant. For the 1:1:1 sample, 1.84 mL of each precursor solution was added. The resulting mixture was then heated to 95 °C under continuous nitrogen flow. Once the temperature reached approximately 95 °C, a mixture of lichen extract (8 mL) and 0.5 M NaOH (1.25 mL), acting as the reducing agent, was added dropwise. The reaction was stirred at 450 rpm for 4 h, then cooled to room temperature. The obtained nanocomposite was filtered and washed three times with ethanol and DI water and then dried in a vacuum oven at 60 °C for 24 h.

Characterization Analysis

Various assays were used to characterize the chemical and morphological features of LrGO-Ag-Au-Cu_xO nanocomposite. UV-Vis spectroscopy (Shimadzu UV-1601) was used to investigate structural and optical properties, photocatalytic, and catalytic activities of the nanocomposites. The samples were also analysed using Fourier-transform infrared spectroscopy (FTIR, model 8400 S Shimadzu), with a scanning range from 400 cm^{-1} to 4000 cm^{-1}. High-contrast Transmission Electron Microscopy (CTEM, FEI Tecnai G2 Spirit BioTwin) was performed at an accelerating voltage of 120 kV using a LaB_6 electron source, with a resolution limit of 0.34 nm. Imaging modes included bright-field and selected area electron diffraction (SAED). A sample tilt and a eucentric goniometer stage were employed to capture multiple crystallographic orientations. Scanning Electron Microscopy (SEM, FEI Quanta 400 F Field Emission SEM) was operated at an accelerating voltage of 30 kV, with a resolution of 1.2 nm. Samples were drop-cast onto aluminium foil-covered stubs. X-ray photoelectron spectroscopy (XPS) analysis was performed using a PHI 5000 VersaProbe (Thermo Scientific K-Alpha) instrument. The X-ray source was monochromatic Al Kα (1486.6 eV), with a beam size adjustable within the range of 10–200 µm. During analysis, the X-ray power was set to 50 W. A dual-beam charge neutralization system was activated to prevent surface charging of insulating samples. The spectrometer operated under ultra-high vacuum conditions, and measurements were carried out at a base pressure of approximately 10^{-9} mbar. The pass energy during data acquisition was set to 20 eV, and the step size was adjusted to 0.1 eV. The photoelectron take-off angle was fixed at 45°. Peak analysis was conducted using Thermo Avantage™ software, and peaks were fitted using a mixed Gaussian–Lorentzian function to ensure optimal deconvolution. X-ray diffraction (XRD) patterns were recorded using a Rigaku MiniFlex 600 diffractometer with Cu-Kα radiation (λ = 1.54056 Å) over a 2θ range of 5–80°, with a step size of 0.02° and a scan rate of 4° min^{-1}. The specific surface area of the synthesized nanocomposite was determined by N_2 adsorption/desorption analysis performed on a Quantachrome NOVA 2200 Gas Adsorption System, based on the Brunauer–Emmett–Teller (BET) theory. Raman spectra were collected using a Thermoscientific DXR Raman microscope with a 633 nm laser excitation wavelength. Post-catalysis TEM images were acquired using a JEOL JEM-100CX II electron microscope at an accelerating voltage of 80 kV.

Catalytic Experiment

The catalytic performance of the LrGO-Ag-Au-Cu_xO nanocomposites was evaluated using the reduction of 4-NP to 4-AP as a model reaction, following the procedure described in our previous work [14]. In brief, a freshly prepared aqueous 4-NP solution (9.52 mL, 9.6×10^{-5} M) was mixed with $NaBH_4$ solution (0.48 mL, 0.1 M), resulting in a $NaBH_4$/4-NP molar ratio of 52.5, and 2.7 mL of the mixture was transferred to a quartz cuvette. The reaction was started by adding 200 µL of catalyst suspension (0.5 mg catalyst). The progress was monitored using UV–Vis spectroscopy (Shimadzu UV-1601) in the 200–500 nm range at room temperature, with a 2 nm sampling interval and a minimum spectrum acquisition time of 18 s. For reusability tests, after each catalytic run, the reaction mixture was centrifuged to recover the catalyst. The collected catalyst was washed once with deionized water and then reused in a fresh 4-NP/$NaBH_4$ solution under the same conditions. This process was repeated for 11 consecutive cycles.

Photocatalytic Experiment

After confirming the catalytic activity and reusability, the photocatalytic efficiency of the nanocomposite was further examined for the degradation of MB dye under visible light irradiation. Photocatalytic experiments were performed

under visible LED light using a Luminus CXM-18 COB Arrays White LED as the light source at room temperature, with an emitting surface diameter of 17.5 mm and an irradiance of 570 W m^{-2}. The experimental solution was prepared by diluting a stock dye concentration of 2 mM to achieve a final concentration of 10 ppm of MB, resulting in a total solution volume of 40 mL. The photocatalytic experiment was repeated 3 times.

A total of 10 mg of the LrGO-Ag-Au-Cu_xO nanocomposite served as the photocatalyst. Prior to irradiation, a preliminary 3-hour dark experiment was conducted to determine the adsorption-desorption equilibrium. As the results indicated, the system reached equilibrium in approximately 45 min (Figure S2); accordingly, this duration was fixed for all subsequent experiments. The solution was stirred in the dark for 45 min using a magnetic stirrer to ensure adsorption-desorption equilibrium between the catalyst and MB. Samples (800 µL each) were taken from the mixture at regular intervals, then centrifuged at 10,000 rpm for 8 min to remove the catalyst. The absorbance spectrum of the solution was then analyzed using a UV-Vis spectrometer (Shimadzu UV-1601) to monitor the decrease in dye concentration at 664 nm [15].

Determination of Band Gap and Band Properties

UV-Vis spectra of Cu_xO, LrGO, LrGO-Ag, and LrGO-Ag-Au nanocomposites were recorded, and band gap values were calculated from Tauc plots. The band properties were further investigated by Mott–Schottky analysis using a Gamry Reference 3000 potentiostat-galvanostat with a three-electrode configuration (counter electrode: platinum wire, reference electrode: Ag/AgCl, working electrode: glassy carbon electrode) and 0.1 M Na_2SO_4 as the electrolyte solution. For the preparation of the working electrode, 4 mg of the nanocomposite was dispersed in 2 mL of an equivolume deionized water-ethanol mixture. Subsequently, 20 µL of Nafion was added and the solution was sonicated for 20 min. Finally, 10 µL of the above solution was drop-cast onto the glassy carbon electrode and dried in a vacuum oven at 60 °C for 24 h.

Statistical Analysis

All catalytic and photocatalytic experiments were performed in triplicate ($n=3$), and the results are reported as mean ± standard deviation (mean ± SD). The error bars in the figures represent the standard deviation, indicating measurement variability. All data processing and statistical analyses were carried out using OriginPro (OriginLab, USA).

Results and Discussion

The LrGO-Ag-Au-Cu_xO nanocomposite was synthesized utilizing Cetraria islandica (L.) Ach. as a green reducing and stabilizing agent. GO and inorganic metal salts in aqueous solution were reduced by an extract from *Cetraria islandica (L.)* Ach., which acted both as a bioinorganic reducing agent for the oxygenated functional groups of GO and for the inorganic metal ions adsorbed on the GO surface, producing Ag, Au, and Cu_xO nanoparticles on LrGO, and as a stabilizing agent for the resulting deoxygenated rGO nanosheets, thereby imparting strong hydrophobic properties to the material and preventing further growth of metal and metal oxide nanoparticles [14, 17] (Figure S1). In this process, $AgNO_3$, $HAuCl_4$, and $CuSO_4$ solutions were employed at various molar ratios ($AgNO_3$:$HAuCl_4$:$CuSO_4$; 0.25:0.25:1, 0.5:0.5:1, 1:1:1, 1:1:2, and 1:1:4). The samples were designated as LrGO-Ag-Au-Cu_xO (0.25:0.25:1), LrGO-Ag-Au-Cu_xO (0.5:0.5:1), LrGO-Ag-Au-Cu_xO (1:1:1), LrGO-Ag-Au-Cu_xO (1:1:2), and LrGO-Ag-Au-Cu_xO (1:1:4), respectively.

Characterization of LrGO-Ag-Au-Cu_xO

The UV-Vis and FTIR spectra of LrGO-Ag-Au-Cu_xO nanocomposites synthesized using a green synthesis approach with different molar ratios of metal ions are presented in Fig. 1. During the synthesis process, GO in the initial solution undergoes reduction, resulting in the formation of reduced graphene oxide. This occurs through the loss of oxygen-containing functional groups in GO during the reduction process. The mechanism by which lichen-based bio-reducing agents convert GO to LrGO is attributed to the reduction capacity of phenolic components and organic acids. It has been reported that phenolic components contribute to the reduction of GO through electron transfer mechanisms while also modifying the surface chemistry of the resulting LrGO. The loss of C=O and C-OH groups, along with the reorganization of the π-network structure, is accompanied by the formation of reduced graphene oxide [14, 16].

The confirmation of this reduction is provided by the UV-Vis spectra of GO in Figure S3, which exhibits two characteristic peaks: the $\pi \rightarrow \pi^*$ transition of aromatic C=C bonds at 232 nm and the $n \rightarrow \pi^*$ transition of C=O groups at 304 nm. The reduction degree of GO is directly related to the nature and concentration of the reducing agent used. The UV–Vis spectra confirmed the reduction of GO, as evidenced by red-shift of $\pi \rightarrow \pi^*$ transition peak from 232 nm to 270–290 nm and disappearance of the $n \rightarrow \pi^*$ peak at 304 nm. Natural reducing agents such as the extract of *C. islandica (L.) Ach.* facilitate the deoxygenation process of GO, leading to the

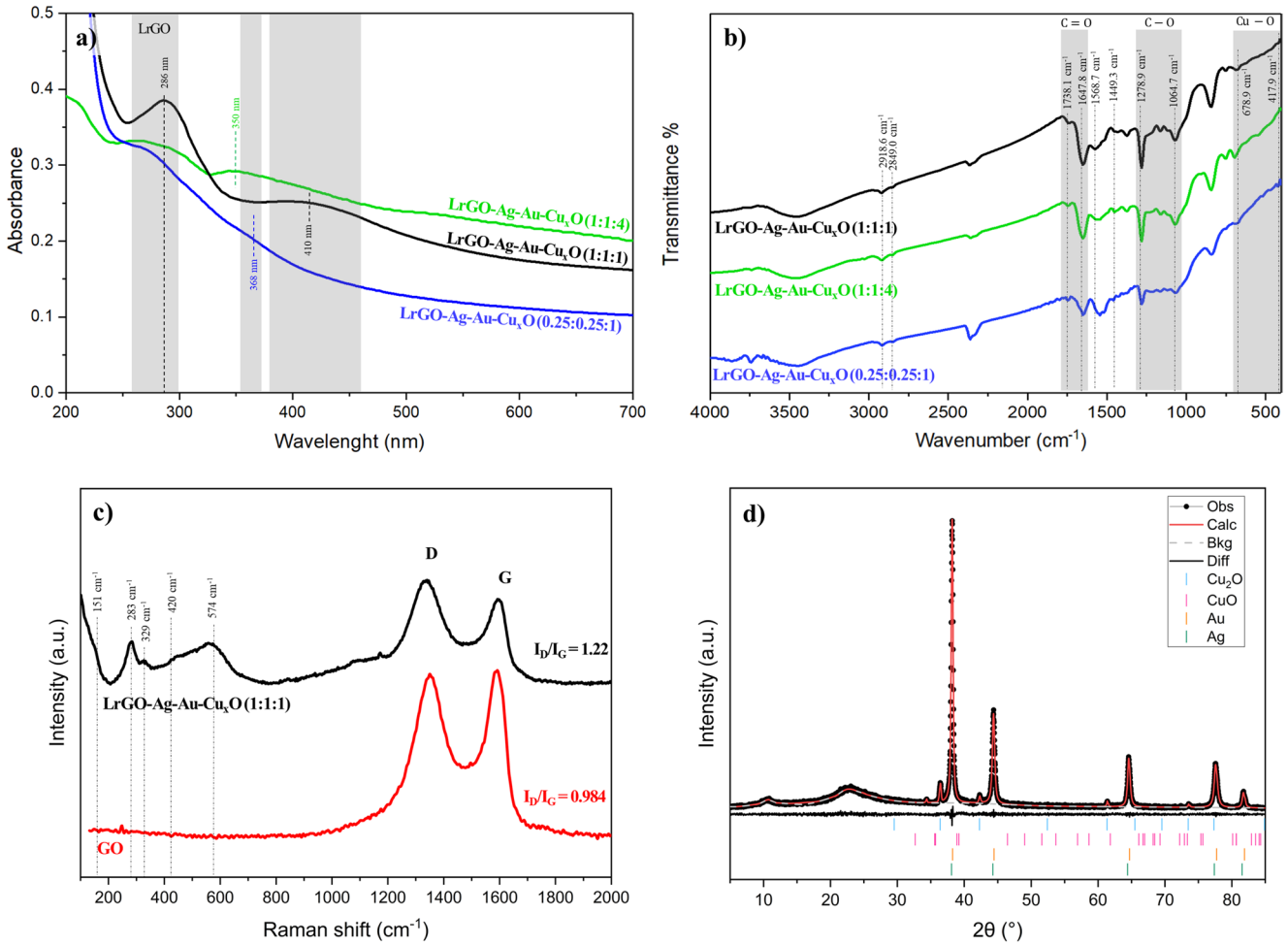


Fig. 1 (**a**) UV-Vis spectra and (**b**) FTIR spectra of LrGO-Ag-Au-Cu_xO nanocomposites with molar ratios (1:1:1), (1:1:4), and (0.25:0.25:1); (**c**) Raman spectra of GO and LrGO–Ag–Au–Cu_xO (1:1:1);(**d**) XRD pattern with Rietveld refinement profile of the LrGO–Ag–Au–Cu_xO (1:1:1) nanocomposite

elimination of C = O groups. As shown in Fig. 1a, following reduction, the n→π* peak at 304 nm disappears completely, while the π→π* transition peak undergoes a redshift from 232 nm to a broad peak centered at approximately 286 nm (270–290 nm range), indicating significant restoration of the graphene π-network structure[14, 17, 16]. In addition to the characteristic bands of GO, the UV-Vis spectra of LrGO-Ag-Au-Cu_xO samples with different metal ion molar ratios, shown in Fig. 1a, reveal the emergence of new absorption bands in the range of 340–500 nm due to the reduction process via the green synthesis approach. These bands are associated with the surface plasmon resonance (SPR) effect of inorganic metallic (Ag, Au) and inorganic metal oxide (CuO, Cu_2O, CuO/Cu_2O) nanoparticles deposited on the LrGO nanosheets, confirming the formation of a multifunctional inorganic–organic hybrid nanocomposite. Specifically, Ag nanoparticles exhibit an SPR band within the 400–450 nm range, while Au nanoparticles display an SPR band between 500 and 550 nm [17]. For copper oxides, characteristic absorption peaks, particularly those corresponding to CuO, Cu_2O, and CuO/Cu_2O composites, are observed between 300 and 500 nm. Among these, the peak at approximately 380 nm is attributed to the band edge transition of CuO/Cu_2O, highlighting the electronic transitions within these metal oxides [20–21]. The LrGO-Ag-Au-Cu_xO nanocomposite with a 1:1:1 molar ratio exhibits a characteristic absorption band spanning from 380 nm to 450 nm, with a central peak at approximately 410 nm. This peak arises from the combined SPR effects of Ag and Au nanoparticles, along with the characteristic electronic transitions of CuO and Cu_2O, which are typically observed around 380 nm. When the $CuSO_4$ concentration is increased (1:1:4 molar ratio), a pronounced blue shift occurs, leading to the formation of a broad absorption peak centered at 348 nm, accompanied by an additional broad peak around 550 nm. This spectral shift suggests that the increased copper content enhances the CuO and Cu_2O-related transitions in this region. Additionally, the SPR peaks corresponding

to Ag and Au, observed around 500 nm, indicate the formation of a separate metallic phase, further confirming structural changes induced by increased $CuSO_4$ concentration. Conversely, when the $CuSO_4$ concentration is kept constant and the Au and Ag concentrations are reduced (0.25:0.25:1 molar ratio), a weak shoulder peak emerges at approximately 368 nm. This feature is attributed to the Cu_2O-CuO transition. Overall, Cu_2O-CuO transitions remain a defining spectral feature across all compositions. However, as $CuSO_4$ concentration increases, the system tends to form larger and more agglomerated copper-rich structures, leading to a more distinct Cu-related absorption band. In contrast, in compositions with lower Cu content (1:1:1 and 0.25:0.25:1), well-defined nanostructures are formed in a more controlled manner, resulting in a less pronounced Cu-related absorption band. These findings highlight the critical role of copper in dictating both the optical properties and morphological evolution of the nanocomposites.

Figure 1b presents the FTIR spectra of LrGO-Ag-Au-Cu_xO nanocomposites synthesized using lichen, incorporating different molar ratios of metal salts (1:1:1, 0.25:0.25:1, and 1:1:4). For comparison, the FTIR spectrum of GO is provided in Figure S4. In the FTIR spectrum of GO, the broad peak at 3400 cm^{-1} and the sharp peak at 1388.7 cm^{-1} correspond to the O–H stretching vibrations associated with absorbed water molecules and hydroxyl groups. The band observed at 1725.9 cm^{-1} is attributed to the C=O stretching vibration of carboxyl groups, while the peak at 1620.3 cm^{-1} corresponds to C=C stretching vibrations from the unoxidized graphitic domain. Additionally, the band at 1220 cm^{-1} represents C–OH stretching vibrations of hydroxyl groups, whereas the band at 1050 cm^{-1} is assigned to the C–O–C stretching vibrations. During the reduction process, it is expected that these characteristic peaks will either disappear completely or significantly weaken due to the removal of oxygen-containing functional groups [14,19, 20].

Upon analyzing the FTIR spectrum of LrGO-Ag-Au-Cu_xO nanocomposites in Fig. 1b, a noticeable decrease in intensity is observed for peaks corresponding to oxygen-containing functional groups in GO. Some of these peaks have even completely disappeared. This confirms the effective reduction of GO by *Cetraria islandica (L.)* Ach. However, not all functional groups have been entirely eliminated, indicating that certain oxygen-containing functionalities still remain in the structure. Additionally, the FTIR spectrum of *C. islandica* (L.) Ach. is presented in Figure S5. According to the literature, *C. islandica (L.)* Ach. is known to contain a high concentration of polysaccharides and various secondary metabolites. Its FTIR spectrum exhibits absorption bands at 2916.4 and 2854.7 cm^{-1}, corresponding to the C–H stretching vibrations of aliphatic acids; 1743.7 cm^{-1} for the C=O stretching vibration of ester chains; 1697.4 cm^{-1} for phenyl ester C=O stretching; 1651.1 cm^{-1} for aldehyde C=O stretching; 1581.6 cm^{-1} for C=C stretching; 1458.2 cm^{-1} for CH_2 and CH_3 vibration bands; and 1265.3 and 1072 cm^{-1} for C–O stretching vibrations [14, 17, 19]. Similarly, the presence of –OH stretching vibrations due to water molecules in the structure has been detected in the FTIR spectra of both LrGO-Ag-Au-Cu_xO and GO.

The identification of *C. islandica (L.)* Ach. -derived functional groups in the LrGO-Ag-Au-Cu_xO FTIR spectrum confirms the effective interaction of this bio-reducing agent with LrGO-based nanocomposites, contributing to their stabilization. Furthermore, the spectral bands observed in the 400–1000 cm^{-1} range primarily correspond to the vibrational modes of metals and metal oxides. Specifically, the spectral bands at 417.9, and 678.9 cm^{-1} are attributed to Cu–O vibrational modes of CuO and Cu_2O nanoparticles, respectively. The observed shift relative to the reference values reported for CuO (~473–588 cm^{-1}) and Cu_2O (~623–640 cm^{-1}) [21–27] is consistent with nanoparticle size effects and CuO/Cu_2O heterostructure formation on the LrGO surface [17]. These analyses collectively indicate that the LrGO-Ag-Au-Cu_xO nanocomposites synthesized using *C. islandica* (L.) Ach. have undergone a successful reduction process and have been effectively stabilized.

Figure 1c displays the Raman spectra of the GO and LrGO-Ag-Au-Cu_XO (1:1:1). In the Raman spectrum of the GO, the peak located at 1593 cm^{-1} is referred to as the G band, whereas the peak at 1350 cm^{-1} is assigned to the D band. The emergence of the D band is attributed to the reduction in the size of the in-plane sp^2 domains because of extensive oxidation over the graphene structure. The D/G intensity ratio (I_D/I_G) is 0.984 and 1.22 for GO and LrGO-Ag-Au-Cu_XO, respectively. This result indicates that a significant amount of the oxygen-containing functional groups in the GO structure was removed, leading to a substantial restoration of the sp^2 structure of the reduced graphene sheets. Simultaneously, it also suggests a further decrease in the average size of the sp^2 domains due to the deterioration of the crystallinity of the graphitic structure during the reduction process [22]. Furthermore, in the Raman spectrum of LrGO-Ag-Au-Cu_XO, the peaks observed at 283 cm^{-1} (Ag mode), two Bg modes 329 cm^{-1}, and 574 cm^{-1} correspond to the characteristic vibrational peaks of CuO nanostructures formed on the rGO surface [23, 24]. Additionally, a shoulder at approximately 151 cm^{-1} and a peak at 420 cm^{-1} are also observed in the spectrum of LrGO-Ag-Au-Cu_xO, which can be attributed to the characteristic vibrational modes of Cu_2O [25, 26].

The XRD pattern and Rietveld refinement profile of the LrGO–Ag–Au–Cu_xO (1:1:1) nanocomposite are presented in Fig. 1d. The pattern reveals a broad and low-intensity peak centered at approximately $2\theta = 23.06°$, which is

attributed to the (002) plane of LrGO, confirming the successful reduction of GO during the green synthesis process. The successful reduction of GO to LrGO is further supported by the XRD patterns of GO and LrGO provided in Figure S6, where the characteristic GO peak at 2θ = 10.8° (d-spacing = 0.819 nm) disappears upon reduction and shifts to approximately 2θ = 22° (d-spacing = 0.404 nm), approaching the interlayer spacing of pristine graphite (0.34 nm) [14, 16]. Rietveld refinement was performed using GSAS-II software, confirming the presence of four crystalline phases: Ag, Au, CuO, and Cu_2O. The diffraction peaks at 2θ = 38.14°, 44.35°, 64.45°, 77.44° and 81.74° are consistent with the (111), (200), (220), (311) and (222) planes of face-centered cubic Ag (COD 1100136) and Au (COD 1100138), whose characteristic reflections overlap due to their similar lattice parameters. The diffraction peaks at 2θ = 38.14°, 44.35°, 64.45°, and 77.44° are assigned to the (111), (200), (220), and (311) planes of face-centered cubic Ag and Au phases, respectively. The peaks at 2θ = 36.42°, 42.31°, 61.35°, and 73.50° are attributed to the (111), (200), (220), and (311) planes of cubic Cu_2O (COD 1000063). The peaks at 2θ = 61.85° and 73.38° correspond to the (11 − 3) and (221) planes of monoclinic CuO (COD 1011148), with additional CuO reflections at 2θ = 38.94° and 39.22° corresponding to the (111) and (200) planes, overlapping with the Ag/Au diffraction region. The refined lattice parameters are as follows: Ag (cubic, a = 4.08525 Å), Au (cubic, a = 4.06926 Å), CuO (monoclinic, a = 4.64979 Å, b = 3.41079 Å, c = 5.11189 Å), and Cu_2O (cubic, a = 4.26853 Å) [27]. The phase weight fractions obtained from the refinement indicate that Ag is the dominant phase (56.9 wt%), followed by Au (28.9 wt%), CuO (7.5 wt%), and Cu_2O (6.7 wt%). The goodness of fit parameters, Rwp = 9.635 and χ^2 = 2.591, confirm the reliability of the refinement.

The elemental chemical composition of the surface of LrGO-Ag-Au-Cu_xO nanocomposite was analyzed using XPS. The survey spectra (Fig. 2a) showed the presence of C1s (78.4%), O 1 s (19.9%), Cu 2p (0.8%), Ag 3 d (0.6%) and Au 4f (0.3%) at 285 eV, 532 eV, 934 eV, 368 eV and 84 eV, respectively. The C1s spectrum exhibited four distinct peaks corresponding to C-C, C-O, C = O, and O-C = O at 284.36, 286.1, 287.29, and 288.56 eV, respectively (Fig. 2b). The presence of these oxygen-containing functional groups (C = O and C–O) is attributed to the incorporation of lichen extract and residual oxygenated functional groups during the chemical reduction. The extract of *Cetraria islandica* (L.) Ach. is rich in polysaccharides, secondary metabolites, and other components which not only contribute to the reduction process but also serve as stabilizers for the rGO layers and metal/metal oxide nanoparticles [14]. The oxygen-rich compounds derived from the lichen act as reducing and capping agents, facilitating efficient reduction of GO to rGO, while preserving functional oxygen groups crucial for enhancing catalytic activity. Figure 2c and d illustrate the deconvolution of Au 4f and Ag 3 d spectra, respectively. In Fig. 2c, the deconvolution of Au 4f reveals peaks at Au $4f_{7/2}$ (84.0 eV) and Au $4f_{5/2}$ (87.7 eV), which are associated with elemental gold (Au^0). This finding confirms that metallic gold is the predominant oxidation state within the sample, as further supported by the spin-orbit splitting of 3.7 eV [34–29]. Similarly, Fig. 2d displays the deconvolution of Ag 3 d, showing peaks at 368.17 eV (Ag $3d_{5/2}$) and 374.19 eV (Ag $3d_{3/2}$), with a spin-orbit splitting of 6.02 eV. These binding energies are in excellent agreement with reported values for metallic silver (Ag $3d_{5/2}$: 368.18 eV, Ag $3d_{3/2}$: 374.18 eV, spin-orbit splitting: 6.0 eV), confirming the zero-valent oxidation state of Ag in the nanocomposite [37, 38]. Notably, Ag^+ species would be expected at significantly lower binding energies (~366.8 eV), which was not observed in the present spectra [39]. The observed minor shift relative to bulk silver may be attributed to charge transfer interactions between Ag and the surrounding Au and LrGO matrix, as reported for similar bimetallic nanostructures [40]. The XPS spectrum of Cu 2p, as shown in Fig. 2e, revealed peaks at 953.9 eV and 934.3 eV. The fitted peaks at 954.3 eV and 934.6 eV are attributed to CuO, whereas peaks at 952.6 eV and 933.2 eV indicate the presence of Cu_2O [34–43].

The presence of two shake-up satellite peaks further supports the presence of CuO. Consequently, these XPS results indicate that Cu_2O is present in the form of CuO/Cu_2O inorganic heterojunctions within the LrGO–Ag–Au–Cu_xO nanocomposite. Furthermore, Mott-Schottky analysis corroborated the presence of a significant amount of CuO intermixed with Cu_2O in the nanocomposite. Consistent with these findings, Rietveld refinement of the XRD pattern (Fig. 1d) independently confirmed the coexistence of both CuO (7.5 wt%) and Cu_2O (6.7 wt%) phases, along with metallic Ag (56.9 wt%) and Au (28.9 wt%), providing crystallographic evidence that fully supports the XPS assignments. Overall, the identification of these metallic and oxidized forms of Au, Ag, and Cu in the XPS spectra confirms the successful reduction of both gold and silver to their metallic states, alongside the coexistence of CuO and Cu_2O heterojunctions. This highlights the effective incorporation of metal species in the LrGO-Ag-Au-Cu_xO nanocomposite, contributing to its enhanced catalytic performance.

The morphological properties of the LrGO-Ag-Au-Cu_xO (1:1:1) nanocomposites were examined with FE-SEM and CTEM. Figure 3a and b present the FE-SEM images depicting the LrGO-Ag-Au-Cu_xO (1:1:1) nanocomposite. The FE-SEM images display Cu_xO (CuO/Cu_2O) nanorods, and Ag and Au nanoparticles effectively coating the surface of crumpled and corrugated LrGO nanosheets. The presence of peaks corresponding to C, O, Cu, Ag, and Au in the EDX

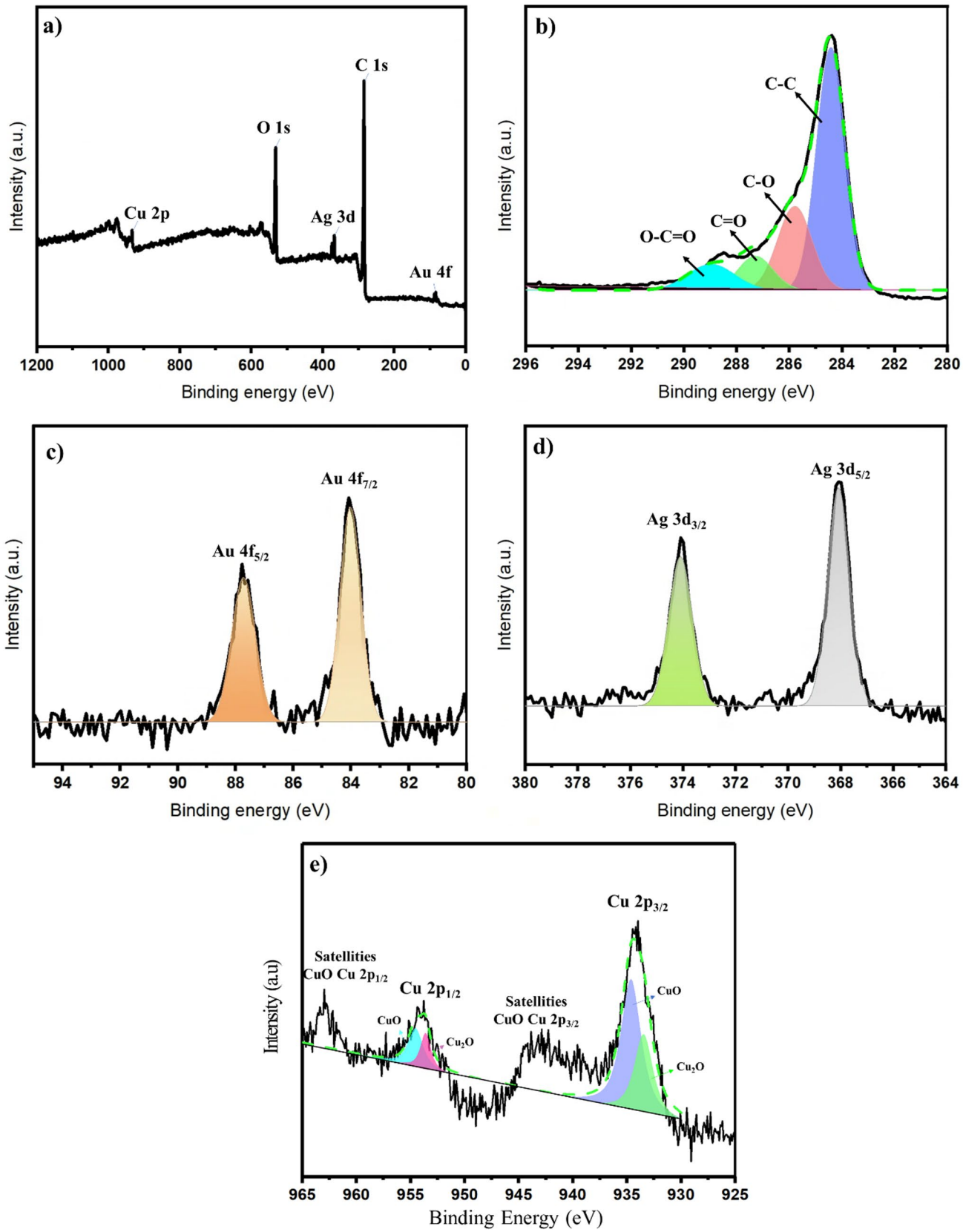


Fig. 2 XPS spectra of LrGO-Ag-Au-Cu_xO (1:1:1) nanocomposite; (**a**) survey spectra, (**b**) C 1s, (**c**) Au 4f, (**d**) Ag 3d, and (**e**) Cu 2p peaks

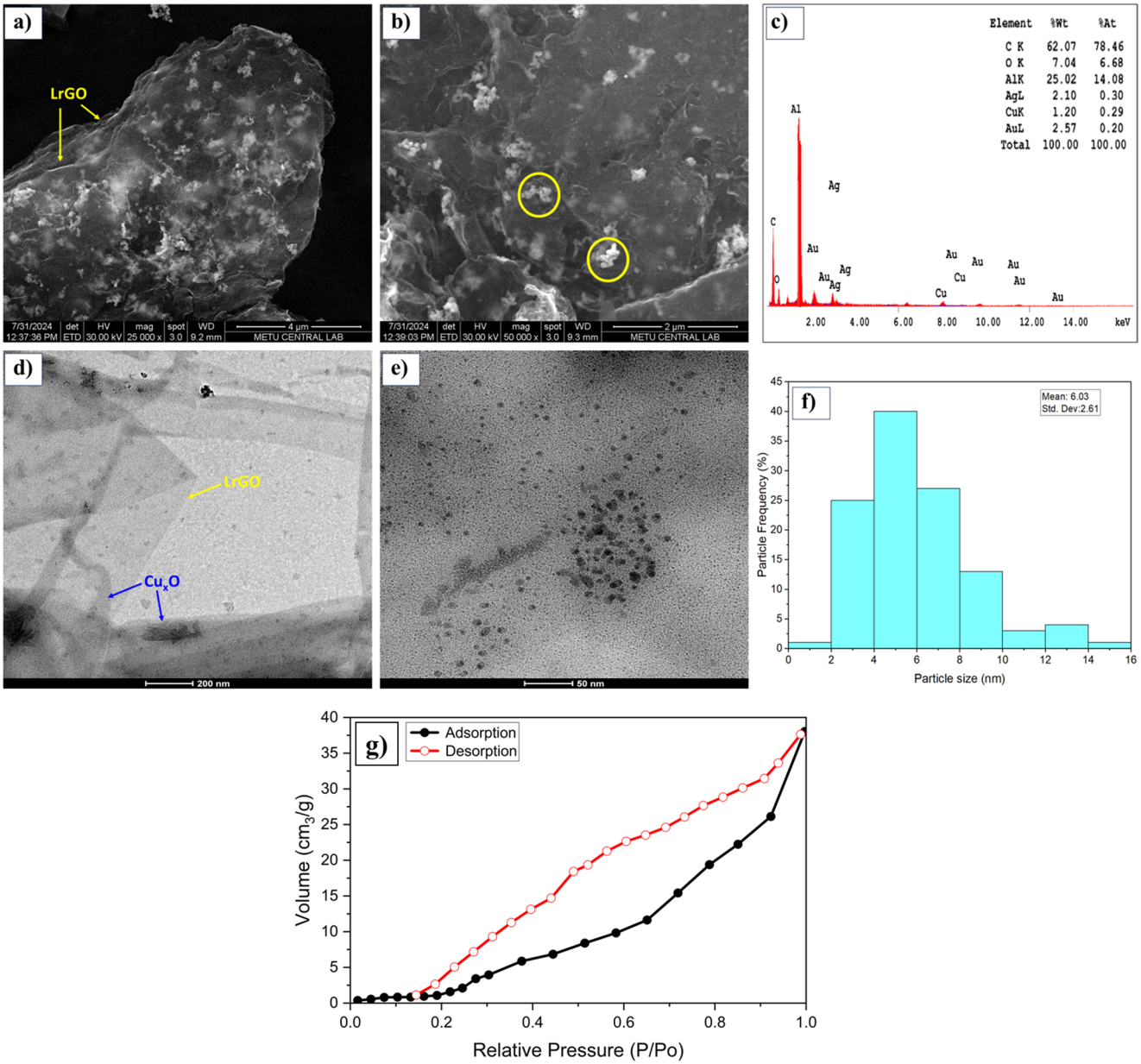


Fig. 3 (**a**, **b**) Fe-SEM and (**d**, **e**) TEM images of LrGO-Ag-Au-Cu_xO (1:1:1) nanocomposite, (**c**) EDX spectra, (**f**) particle size distribution histogram, and (**g**) N_2 adsorption-desorption isotherm of LrGO-Ag-Au-Cu_xO (1:1:1) nanocomposite

spectra **(inset** Fig. 3c**)** further confirms the successful synthesis of the LrGO-Ag-Au-Cu_xO nanocomposite.

Figure 3d and e show TEM images depicting the LrGO-Ag-Au-Cu_xO (1:1:1) nanocomposite. The TEM images also indicate successful synthesis of the Cu_xO nanorods along with Ag and Au nanoparticles with small size and narrow particle distribution. Figure 3f presents the particle size distribution histogram of Ag and Au nanoparticles in the LrGO-Ag-Au-Cu_xO nanocomposite. The histogram, obtained from TEM analysis, shows that the particle sizes range from approximately 2 to 14 nm, with an average size of 6.03 nm and a standard deviation of ± 2.61 nm. The distribution indicates that most nanoparticles are within the 4–8 nm range, with a peak frequency around 6 nm.

The N_2 adsorption-desorption isotherm of the LrGO–Ag–Au–Cu_xO (1:1:1) nanocomposite is presented in Fig. 3g. The isotherm exhibits Type V characteristics, as evidenced by the absence of a distinct knee at low relative pressures and the gradual, convex adsorption profile at $P/P_o < 0.2$, indicative of weak adsorbent–adsorbate interactions in the low-pressure region. At higher relative pressures, a pronounced uptake accompanied by a wide hysteresis loop is observed, consistent with molecular clustering followed by pore filling, as described for Type V isotherms in

the IUPAC classification [37–46]. This behavior is consistent with the layered architecture of the LrGO nanosheets, where restacking and nanoparticle loading may contribute to weak initial N_2 interactions with the composite surface. The BET specific surface area of the nanocomposite was determined to be 11 $m^2 g^{-1}$. This relatively low surface area can be attributed to several factors. First, the dense loading of Ag, Au, and Cu_xO nanoparticles onto the LrGO surface may partially block accessible pore channels and contribute to sheet restacking, as commonly reported for metal nanoparticle-decorated rGO composites [39, 48]. Second, as confirmed by FTIR analysis, lichen-derived organic compounds remain on the nanocomposite surface following synthesis, contributing to stabilization while potentially occupying surface sites and partially restricting pore accessibility. Nevertheless, the uniform distribution of nanoparticles across the LrGO matrix, as confirmed by TEM analysis (Fig. 3d–f), ensures that the available surface remains accessible for reactant adsorption, which may contribute to the observed catalytic and photocatalytic performance. Despite the relatively low BET surface area, the small nanoparticle size (average 6.03 nm, as determined by TEM analysis) and their uniform distribution across the LrGO matrix provide a high density of accessible active sites, which is considered a more critical factor for catalytic performance than bulk surface area alone.

Taken together, the comprehensive characterization of the LrGO–Ag–Au–Cu_xO (1:1:1) nanocomposite through UV-Vis, FTIR, Raman, XRD, XPS, FE-SEM, TEM, EDX, and BET analyses collectively confirm the successful green synthesis of a well-dispersed multifunctional nanocomposite, with identified crystalline phases, controlled nanoparticle size distribution, and accessible surface area, providing a solid foundation for the catalytic and photocatalytic applications discussed in the following sections.

Catalytic Performance

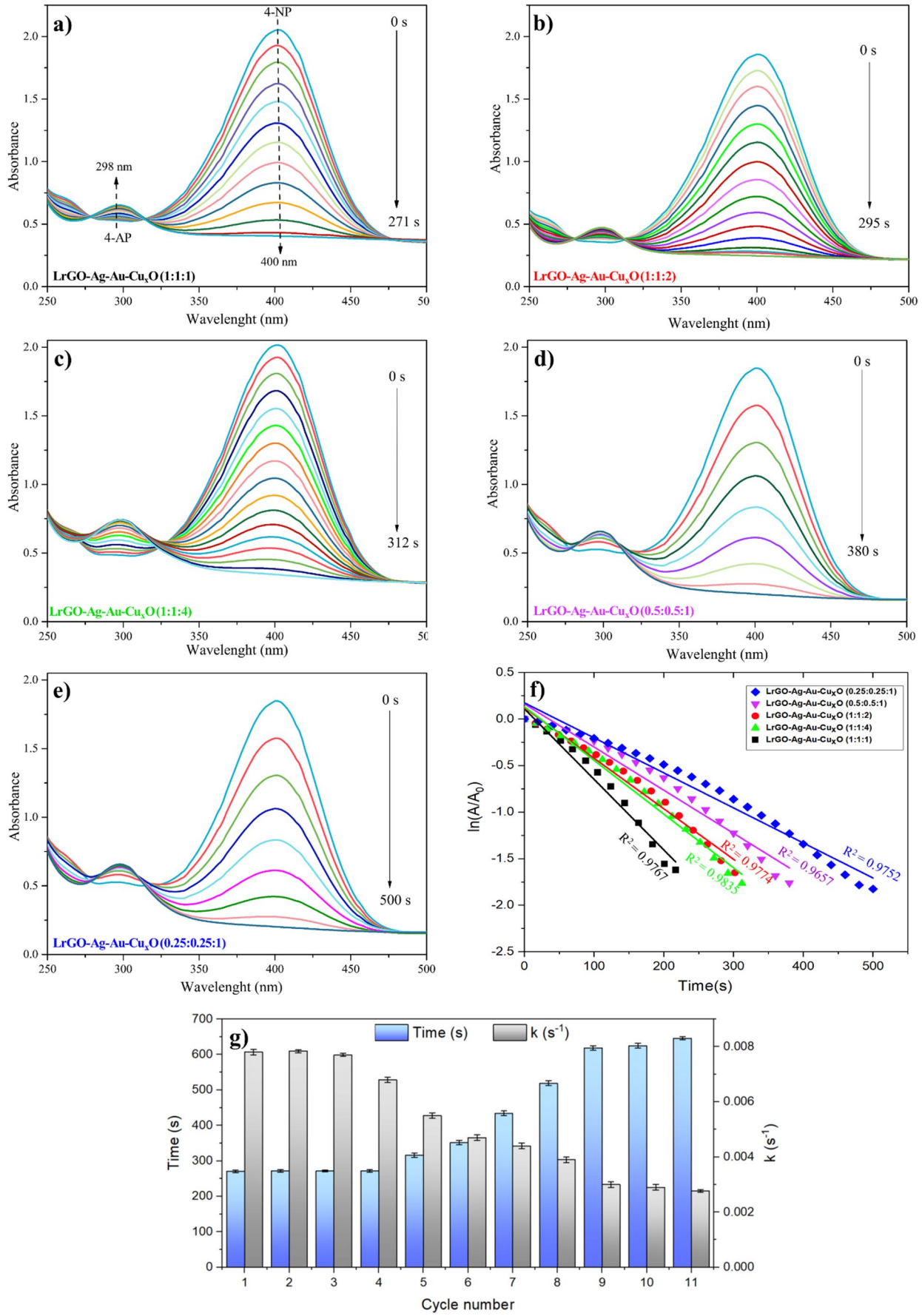
Inorganic metal and metal-oxide nanoparticle-based nanocomposites are essential catalysts for various chemical reactions. They represent a primary research area in inorganic and materials chemistry. This study assesses the catalytic performance of LrGO-Ag-Au-Cu_xO nanocomposites with different compositions. We investigated the catalytic reduction of 4-NP to 4-AP as a model reaction, employing $NaBH_4$ as the reducing agent. This reaction, commonly used as a model system, is thermodynamically favorable because of the difference in standard reduction potentials between the 4-NP/4-AP (−0.76 V) and H_3BO_3/BH_4^- (−1.33 V) redox couples [49, 41]. However, it remains kinetically hindered without a catalyst. This kinetic barrier mainly results from electrostatic repulsion between negatively charged species, such as NP^- and BH_4^-. This repulsion prevents direct electron transfer from $NaBH_4$ to 4-NP in solution [41, 42].

Fig. 4 Time-dependent UV–Vis spectra for the catalytic reduction of 4-NP by $NaBH_4$ in the presence of LrGO-Ag-Au-Cu_xO nanocomposites with different compositions: (**a**) 1:1:1, (**b**) 1:1:2, (**c**) 1:1:4, (**d**) 0.5:0.5:1, and (**e**) 0.25:0.25:1. (**f**) Linear plots of $\ln(A_t/A_0)$ versus time for the corresponding samples. (**g**) Reusability performance of the 1:1:1 nanocomposite over consecutive cycles, showing variation in reduction time and apparent rate constant (**k**)

To clarify the roles of the reducing agent and the catalyst surface, two control experiments were conducted. First, UV–Vis spectra of the 4-NP solution and the 4-NP plus $NaBH_4$ system were recorded over seven days (Figure S7a). The spectra showed minimal changes in absorbance and peak position, indicating system stability and the lack of spontaneous reduction without a catalyst. Quantitatively, the absorbance decreased only slightly (−0.12% at 30 min, −0.24% at 1 h, and −1.44% after 7 days), further confirming the stability of the system. Additional controls evaluated adsorption by monitoring the UV–Vis spectra of the 4-NP-catalyst system (without $NaBH_4$) over three days (Figure S7b). No observable spectral changes were detected, confirming that neither adsorption-driven transformation nor spontaneous reduction occurs in the absence of $NaBH_4$. Quantitatively, only minor fluctuations in absorbance were observed (−3.45% at 30 min, −1.82% at 1 h, and −5.86% after 3 days), supporting negligible adsorption effects. These findings demonstrate that both the reducing agent and the catalyst surface are necessary to initiate the reaction.

Previous studies demonstrate that the reduction mechanism follows a Langmuir–Hinshelwood-type pathway. Both NP^- and BH_4^- species adsorb onto the catalyst surface. Electron transfer occurs through surface-mediated processes involving adsorbed intermediates [43–44]. With an appropriate catalyst, this kinetic barrier is overcome by facilitated electron transfer from adsorbed BH_4^- species to NP^- molecules on the catalyst surface. This allows the catalytic reduction of 4-NP. Using this mechanistic framework, we systematically assessed and compared the catalytic efficacy of the synthesized nanocomposites using UV–Vis spectroscopy.

Figure 4a–e presents the UV–Vis spectra over time for the reduction of 4-NP by LrGO-Ag-Au-Cu_xO nanocomposites in different ratios: (1:1:1), (1:1:2), (1:1:4), (0.25:0.25:1), and (0.5:0.5:1). Adding the catalysts led to a gradual decline in the 4-NP peak at 400 nm and the appearance of a new 298 nm peak for 4-AP. These changes reflect the reduction process, not just physical adsorption. For all compositions, the 4-NP absorption intensity decreased over a finite time, indicating effective catalytic activity. The reduction finished in about 271, 295, 312, 380, and 500 s for the (1:1:1), (1:1:2), (1:1:4), (0.5:0.5:1), and (0.25:0.25:1) samples, respectively. The sample with a molar ratio of


a)
4-NP
0 s
298 nm
4-AP
271 s
400 nm
LrGO-Ag-Au-CuxO(1:1:1)
Absorbance
Wavelenght (nm)
b)
0 s
295 s
LrGO-Ag-Au-CuxO(1:1:2)
c)
0 s
312 s
LrGO-Ag-Au-CuxO(1:1:4)
d)
0 s
380 s
LrGO-Ag-Au-CuxO(0.5:0.5:1)
e)
0 s
500 s
LrGO-Ag-Au-CuxO(0.25:0.25:1)
f)
LrGO-Ag-Au-CuxO (0.25:0.25:1)
LrGO-Ag-Au-CuxO (0.5:0.5:1)
LrGO-Ag-Au-CuxO (1:1:2)
LrGO-Ag-Au-CuxO (1:1:4)
LrGO-Ag-Au-CuxO (1:1:1)
ln(A/A0)
R2 = 0.9752
R2 = 0.9657
R2 = 0.9774
R2 = 0.9835
R2 = 0.9767
Time(s)
g)
Time (s)
k (s-1)
Cycle number

($AgNO_3$:$HAuCl_4$:$CuSO_4$) = 1:1:1 displayed the fastest reduction under the same conditions.

Excess $NaBH_4$ in the 4-NP reduction system allows treatment under pseudo-first-order conditions with respect to 4-NP, since the $NaBH_4$ concentration remains constant [17]. To investigate the kinetic behavior, we monitored the decrease in 4-NP absorbance at 400 nm over time. According to the Beer–Lambert law, absorbance at this wavelength is proportional to the 4-NP concentration. Thus, plotting $\ln(A_t/A_0)$ versus time yields a straight line, demonstrating pseudo-first-order kinetics, as illustrated in Fig. 4f. The apparent rate constant (k) was calculated from the slope of the fitted line, using Eq. 1:

$$ln\left(A_t/A_o\right) = -k.t \quad (1)$$

Here, A_0 represents the initial absorbance of 4-NP at t = 0, while A_t corresponds to the absorbance at reaction time t (sec). The spectra and plots in Fig. 4a–f show the reaction's progress and pseudo-first-order kinetic behavior. Linear equations, correlation coefficients (R^2), and reduction times from $\ln(A_t/A_0)$ versus time fitting are summed in Table S1. The linear plots in Fig. 4f are from individual experimental runs. The k used for comparison was found from three independent measurements and reported as mean ± standard deviation in Table S1. The calculated k values for (1:1:1), (1:1:2), (1:1:4), (0.5:0.5:1), and (0.25:0.25:1) samples are 0.0078 ± 0.0003, 0.0054 ± 0.0002, 0.0058 ± 0.0002, 0.0048 ± 0.0003, and 0.0038 ± 0.0002 s^{-1}, respectively. The nanocomposite sample with a molar ratio of $AgNO_3$:$HAuCl_4$:$CuSO_4$ of 1:1:1 had the highest average k value, consistent with its shorter reduction time.

After evaluating the initial activity, the catalytic performance of the 1:1:1 sample was tested again under the same reaction conditions. Results are shown in Fig. 4g. Each cycle's reduction time and apparent rate constant are compared side by side. The catalyst's performance stayed relatively stable during the early cycles. In later cycles, reduction time grew, and k decreased. These results match the previously observed highest catalytic activity. They also show that the catalyst remains active over several cycles, though performance declines with repeated use.

Cu_xO NPs have been extensively studied for their catalytic activity in various reduction reactions and their relatively low cost compared to noble metals such as Ag and Au. Despite these benefits, their high surface energy leads to aggregation and reduced stability, significantly reducing the number of available active sites. To overcome these issues, researchers often incorporate Cu_xO into composite structures, improving both particle dispersion and structural stability [44–57]. The incorporation of Ag and Au species into Cu-based systems has been shown to influence catalytic behavior through synergistic effects. These metals can promote electron transfer processes and alter surface adsorption properties, thereby impacting overall reaction kinetics. Specifically, Ag is linked to enhanced charge redistribution, while Au can modify adsorption–desorption dynamics, both of which help improve catalytic performance [14, 17, 16].

Compared to other CuO-based composites, the LrGO–Ag–Au–Cu_xO structure may also benefit from the conductive rGO matrix, which offers a high-surface-area platform for dispersing metallic and metal-oxide nanoparticles. As shown by the TEM analysis (Fig. 3d–f), the Cu_xO, Ag, and Au nanoparticles in the composite are relatively small, ranging from 2 to 14 nm, with an average of 6.03 ± 2.61 nm and a peak around 6 nm, indicating effective and uniform dispersion on the LrGO surface. This level of size reduction marks a significant improvement over our previous study [17], where Ag and Au nanoparticles synthesized under similar conditions using the same *Cetraria islandica* extract—but without rGO support— showed a mean particle size of 13 nm, with a broader range of 6–21 nm. The decrease in average particle size from approximately 13 nm to about 6 nm in the current system strongly indicates that the LrGO matrix actively limits particle growth and prevents aggregation during synthesis, thus maintaining a more uniform nanoscale size distribution. This significant reduction in average particle size suggests that the LrGO matrix plays an active role in controlling particle growth during synthesis, which contributed positively to the catalytic performance of the nanocomposite.

Although rGO itself does not exhibit significant intrinsic catalytic activity for the reduction reaction under review, its conductive network may facilitate electron transfer between active metal/metal oxide sites and the reactants [47]. The presence of Ag, Au, and Cu_xO phases on the LrGO surface may therefore enhance interfacial interactions and collectively contribute to the observed catalytic behavior. However, the individual contribution of each component cannot be quantitatively decoupled within the scope of this study, and the observed activity is best interpreted as a result of their collective synergistic interaction.

The catalytic activity of the LrGO–Ag–Au–Cu_xO nanocomposite was evaluated for the reduction of 4-NP and benchmarked against previously reported systems (Table S2). The sample with an Ag: Au: Cu_xO molar ratio of 1:1:1 exhibited an apparent rate constant of k = 0.0078 ± 0.0003 s^{-1} with a total reaction time of 271 s. When positioned within the broader landscape of literature data summarized in Table S2, this performance falls within the range reported for Cu-based and hybrid nanocomposites.

It is important to note that direct cross-study comparisons are inherently limited because of differences in experimental parameters such as initial 4-NP concentration, $NaBH_4$ molar

ratio, catalyst loading, and reaction volume. For example, several systems listed in Table S2 show higher rate constants; however, these values are typically achieved under significantly higher catalyst loadings (e.g., 0.273–0.8 mg mL^{-1}) or very different reaction conditions. Conversely, the present study uses a relatively low catalyst loading (0.172 mg) under moderate conditions, a fact that should be considered when interpreting the kinetic data.

Furthermore, using *Cetraria islandica* extract as the reducing and stabilizing agent offers an environmentally friendly synthesis method, in line with green chemistry principles and consistent with sustainable nanoparticle production strategies documented in the literature [14, 17]. Overall, the catalytic results show that the LrGO–Ag–Au–Cu_xO nanocomposite delivers competitive performance compared to previously reported systems under the given experimental conditions, without needing high catalyst loadings or extreme reaction parameters. After this catalytic assessment, the multifunctional nature of the nanocomposite was further explored through its photocatalytic performance, as discussed in the next section.

Photocatalytic Performance of LrGO-Ag-Au-Cu_xO

Prior to assessing the photocatalytic activity of the LrGO-Ag-Au-Cu_xO inorganic hybrid nanocomposite, the interaction between MB and LED light at room temperature over a period of 180 min was investigated to determine the extent of dye degradation due to the light source alone. The LED source used in this study operates in the 400–700 nm wavelength range with a light intensity of 570 W m^{-2}.

The degradation efficiency was calculated by evaluating the difference between the initial and final absorbance peaks of the MB dye. The efficiency of adsorption and photocatalysis was calculated using the equation:

$$Photocatalytic\ Activity\ \% = (C_0 - C_i)/C_0 = (A_0 - A_i)/A_0 \quad (2)$$

where, C_0 represents the initial concentration, C_t is the concentration at time "t", A_0 is the initial absorbance of the dye and A_t is the absorbance of the dye in solution after time "t".

Figure 5a shows the UV-Vis spectra of MB under LED irradiation in the absence of a catalyst, revealing only the effect of photolysis, which led to a 37% reduction in MB concentration. This reduction was calculated using Eq. 2 and provides a basis for evaluating photocatalytic performance. In this study, MB was chosen as the model contaminant due to its moderate sensitivity to photolysis, allowing for a reliable assessment of the intrinsic activity of the synthesized photocatalysts. To evaluate the efficiency of the synthesized nanocatalysts, the photocatalytic activity of the LrGO–Ag–Au–Cu_xO nanocomposite (1:1:1 metal salt ratio) was investigated. This composition was chosen due to its superior catalytic performance in the reduction of 4-NP. The degradation process was monitored using UV-Vis spectroscopy by tracking the characteristic absorption peak of MB at 664 nm. Upon addition of a photocatalyst under LED irradiation, a gradual decrease in absorbance was observed, indicating the degradation of MB (Fig. 5b). The mean degradation efficiencies were determined as 53.71 ± 2.03%, 70.8 ± 0.45%, 82.5 ± 2.40%, 90.25 ± 3.10%, and 97.67 ± 1.15% at 60, 90, 120, 150, and 180 min, respectively (Fig. 5c). To assess the repeatability and reliability of these results, the experiment was repeated three times and the UV-Vis spectra of each run are provided in Figure S8. Notably, the maximum degradation efficiency observed in individual trials reached 99%, and the low standard deviation values confirm the consistent and reproducible photocatalytic behavior of the nanocomposite. Furthermore, the apparent reaction rate constant of the composite was found to be approximately 10 times higher than that of photolysis, indicating a significant improvement in reaction kinetics. These results demonstrate that the LrGO–Ag–Au–Cu_xO nanocomposite effectively enhances MB degradation under LED irradiation, likely due to improved charge separation and the formation of reactive oxygen species.

The photocatalytic rate constant for the synthesized samples were determined using the relationship between the natural logarithm of the concentration ratio and irradiation time, as described by Eq. 3 and illustrated in Fig. 5d.

$$ln\,(C/C_0) = ln\,(A/A_o) = -\,k_{app}.t \quad (3)$$

Where C_0 is the initial dye concentration (mM), C is the dye concentration at reaction time t (mM), A_o is the initial absorbance, A is the absorbance at reaction time t, k_{app} is the apparent pseudo-first-order reaction rate constant (min^{-1}), and t is the reaction time (min) [48]. The rate constant serves as a key indicator of the photocatalytic activity of the nanocomposites [49].

For LrGO–Ag–Au–Cu_xO, the apparent rate constant was determined as 0.0219 ± 0.00265 min^{-1} across three independent experiments, with individual R^2 values of 0.9905, 0.9881, and 0.9875, confirming good linearity and consistency with pseudo-first-order kinetics. The linear fit shown in Fig. 5d corresponds to the highest-performing trial (k = 0.0246 min^{-1}, R^2 = 0.9905), with the reported rate constant representing the mean of all three independent measurements. For comparison, the apparent rate constant determined under catalyst-free conditions (photolysis only) was 0.0025 min^{-1}, indicating that the nanocomposite enhances the degradation kinetics by approximately 10-fold relative to photolysis alone.

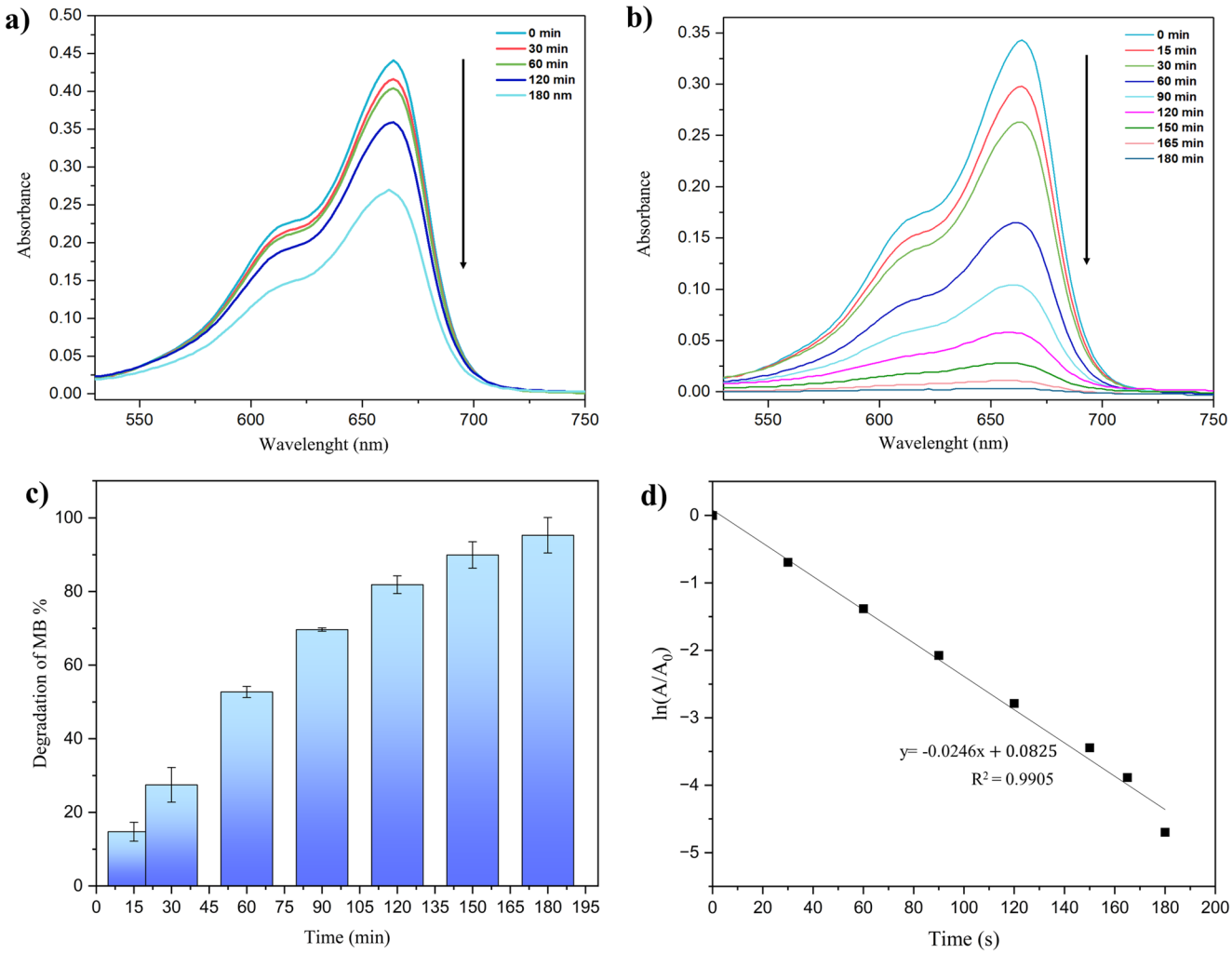


Fig. 5 (**a**) UV-Vis spectra of photocatalytic degradation of MB under LED light in catalyst-free conditions, (**b**) with LrGO-Ag-Au-Cu_xO nanocomposite photocatalyst; (**c**) percent degradation plot of MB versus time, and (**d**) plot of ln (A/A_0) against the duration of irradiation of MB under LED light using LrGO-Ag-Au-Cu_xO (1:1:1) nanocomposite

The photocatalytic performance of the LrGO-Ag-Au-Cu_xO (1:1:1) nanocomposite, which exhibited the highest catalytic efficiency, was thoroughly investigated and summarized in Table S3. With a rate constant of 0.0219 ± 0.00265 min^{-1}, the nanocomposite achieved $97.67 \pm 1.15\%$ degradation efficiency within 180 min, demonstrating its high photocatalytic efficiency in removing organic pollutants such as MB. When compared to previously reported inorganic photocatalytic systems, the LrGO-Ag-Au-Cu_xO (1:1:1) nanocomposite shows competitive performance. CuO-based photocatalysts, such as CuO-GO-TiO_2 (180 min, 64% degradation efficiency) and CuO (120 min, 86.71% degradation efficiency), require significantly longer reaction times and exhibit lower degradation efficiencies. Similarly, other metal oxide-based nanocomposites, such as rGO-Ag-ZnO (120 min, 96% efficiency) and Au/rGO (45 min, 92% efficiency), have demonstrated high degradation efficiencies, but often required larger catalyst amounts or were tested on different organic pollutants. In contrast, with only 10 mg of catalyst, the LrGO-Ag-Au-Cu_xO (1:1:1) nanocomposite demonstrated enhanced photocatalytic performance, achieving higher degradation efficiency with lower catalyst consumption.

The photocatalytic activity of the LrGO–Ag–Au–Cu_xO (1:1:1) nanocomposite is attributed to the synergistic interaction between Ag, Au, and Cu_xO species within the LrGO framework. While conventional Cu_xO-based systems often suffer from rapid charge recombination, this hybrid structure provides an efficient electron transfer pathway that allows for more effective utilization of photogenerated electrons. In this mechanism, the LrGO matrix functions not only as a support but also as an electron mediator and adsorption platform. Due to its high electrical conductivity, rGO acts as an electron transport pathway for electrons from Cu_xO

and metal nanoparticles, facilitating charge separation and reducing recombination losses. The role of charge separation and Schottky barrier interactions in rGO-based multicomponent systems in improving photocatalytic efficiency has been reported in the literature [12, 50]. Consequently, the LrGO matrix extends the lifetime of charge carriers and improves overall photocatalytic performance.

The progression of MB degradation was further confirmed by UV–Vis spectroscopy over the range 200–750 nm. As shown in Figure S9, the characteristic absorbance peak at 664 nm, associated with the π→π* transition in the chromophore group of MB, was almost completely eliminated, reaching 97.67 ± 1.15% degradation efficiency after 180 min of irradiation. The degradation of the dye was further supported by spectral changes in the UV region. The complete disappearance of the peaks at 245 nm and 292 nm, corresponding to the phenothiazine backbone and aromatic ring structures of the MB molecule, indicates successful degradation of the heterocyclic and benzene ring structures [62].

To evaluate the structural integrity of the nanocomposite following photocatalytic use, post-reaction TEM images were recorded (Figure S10). TEM images indicates that the sheet-like morphology of the LrGO support remains preserved. Nanoparticle-rich contrast regions are still observable on the carbonaceous matrix, and no evident large-scale structural collapse was detected, suggesting that the nanocomposite retains its overall morphological integrity after photocatalytic operation.

Following this, Mott-Schottky analysis was performed to better understand the photocatalytic activity of LrGO-Ag-Au-Cu_xO nanocomposite. Mott-Schottky analysis is a valuable technique used to assess the electronic band properties of semiconductors. A photocatalytic reaction reaches completion only when photogenerated charge carriers participate in surface redox reactions, which critically depend on the adsorption and activation of reactants. Semiconductors often play a key role in photocatalytic reactions, as their properties are determined by their electronic band structure. The valence band (VB) is the highest energy level that electrons fill, whereas the conduction band (CB) is the lowest energy level that remains unoccupied by electrons. These two bands are separated by a band gap, an area where no electron states can exist. The band gap contains sub-bands that are closely linked to surface defects and surface states. The band gap energy (E_G) is defined as the energy difference between the lower part of the CB and the upper part of the VB [43, 63].

E_G is crucial in determining the light absorption behaviour of a semiconductor, can be calculated from the UV-Vis spectrum. For the Mott-Schottky analysis, firstly the efficacy of a photocatalyst is closely related to the optical band gap. The optical band gaps were deduced from the absorption spectra by plotting $(\alpha h\upsilon)^{n/2}$ versus photon energy ($h\upsilon$) curves based on the Tauc relation. The relationship between the absorption coefficient (α) and the incident photon energy ($h\upsilon$) is described by **Eq. 4** [43].

$$(\propto h\upsilon) = k(h\upsilon - E_G)^{n/2} \tag{4}$$

where, α is the absorption coefficient, hν is the energy of the incoming photon, n is an integer that helps determine whether the material has direct or indirect electron transitions, and k is a constant. The value of 'n' is 1 for direct band gap transitions and for indirect band gap transitions [42].

As illustrated in Fig. 6, the band gap values for the samples are as follows: LrGO has a band gap of 2.6 eV, LrGO-Ag has a band gap of 1.9 eV, Cu_xO exhibits a band gap of 2.65 eV, the LrGO-Ag-Au composite has a band gap of 1.9 eV. These results indicate that the band gap in the LrGO-Ag-Au-Cu_xO nanocomposite is reduced compared to the individual LrGO, LrGO-Ag, Cu_xO and LrGO-Ag-Au samples.

The positions of the CB and VB edges in a semiconductor photocatalyst can be determined using Eq. 5. These values provide insight into the redox potentials associated with the photogenerated electrons and holes.

$$E_{VB} = E_{CB} + E_G \tag{5}$$

where E_{VB} is the VB edge potential, E_{CB} is the CB edge potential, and E_G is the band gap potential. In the case of an intrinsic semiconductor, the disparity between the CB and flat-band (E_{FB}) potentials can be mathematically described by Eq. 6. In Fig. 7, Mott-Schottky analysis was performed, and the E value was determined and E_{FB} was computed. In the case of n-type semiconductors, the E_{CB} value is typically 0.1 eV more negative than the E_{FB} value. The E_G derived from the Tauc plot can be employed to determine E_{VB} values [43].

E_{FB} can be calculated using the Boltzmann constant (k_B), absolute temperature (T), and elementary charge ($e = 1.602 \times 10^{-19}$ C). Typically, E_{FB} is ascertained through electrochemical impedance spectroscopy (EIS) measurements. The Mott-Schottky (M-S) plot, illustrating the linear relationship between $1/C^2$ and the applied potential, conforms to the Mott-Schottky equation (Eq. 6) for an n-type semiconductor [43]. Mott-Schottky analysis of the synthesized nanomaterials is given in Fig. 7.

$$1/C^2 = (2/(\epsilon_s.\epsilon_0.e.N_D)) \times (E - E_{FB} - (k_B.T/e) \tag{6}$$

Mott-Schottky analyses were conducted on various nanomaterials, including LrGO-Ag-Au, and Cu_xO. The flat-band

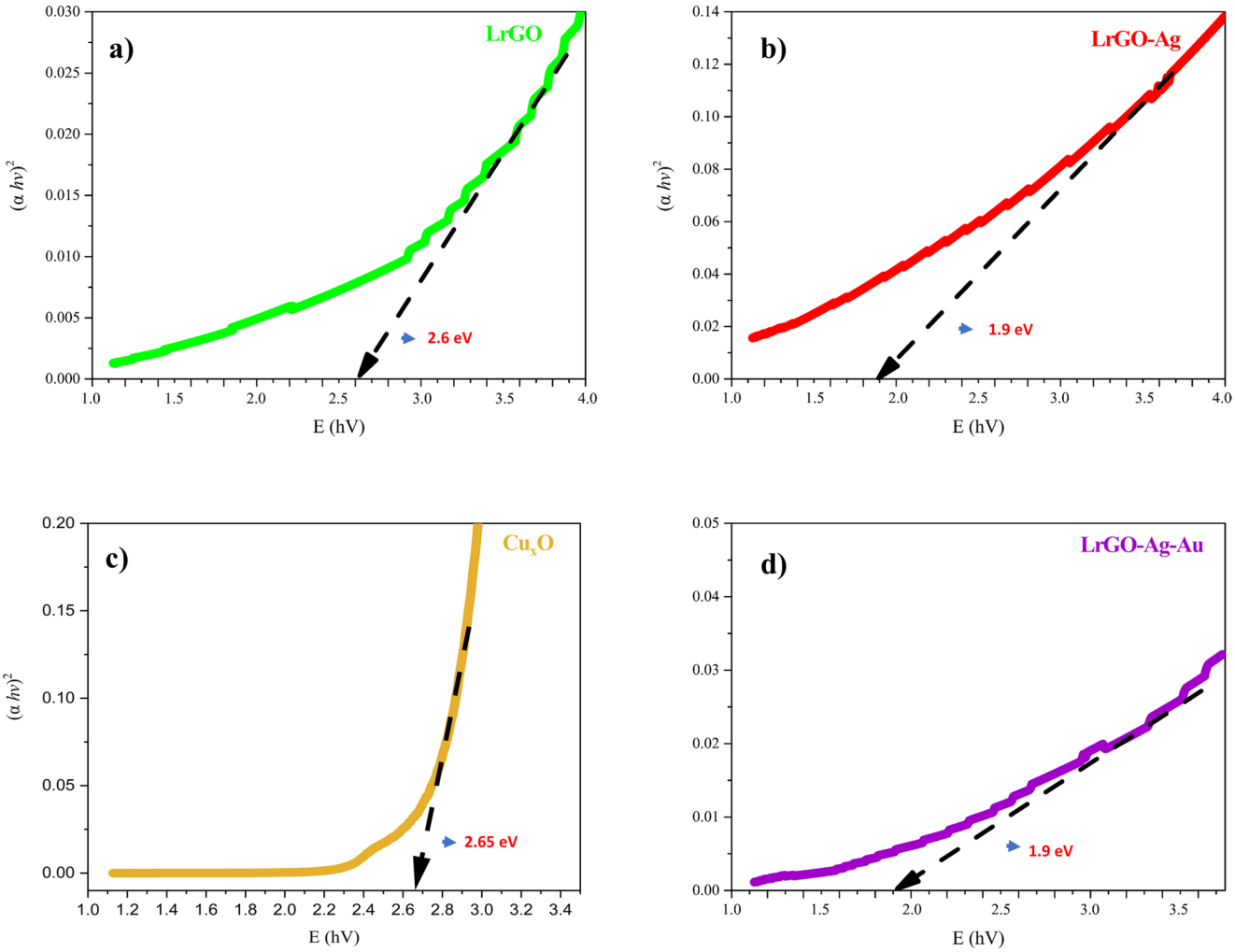


Fig. 6 Tauc plots of (**a**) LrGO, (**b**) LrGO-Ag, (**c**) Cu_xO, and (**d**) LrGO-Ag-Au

potentials of these materials were determined by calculating the x-intercepts of the linear region, resulting in values of −0.375 eV for LrGO-Ag-Au, −1.30 eV for Cu_xO. Cu_xO is a abundant, cost-effective, and environmentally friendly direct band gap semiconductor, with E_G ranging from 1.9 to 2.2 eV. It is being studied for potential applications in photovoltaic and photoelectrochemical devices [64]. It is reported that Cu_xO structures can give a single CB edge [65].

Metal and metal oxides are widely used in various applications, including environmental remediation and electronics, due to their ability to generate charge carriers under light exposure. These materials exhibit unique properties such as well-defined electronic band structures, high light absorption capabilities, and efficient charge transport properties [66]. Semiconductor-assisted photocatalysis has gained significant attention for its ability to address rapid charge recombination issues. To evaluate the photocatalytic potential of the synthesized nanocomposites, their E_{CB} and E_{VB} edge positions were determined. In the calculations, the E_{CB} value of n-type Cu_xO was found to be −1.43 eV, the E_{VB} value was 1.22 eV. The E_{CB} value of LrGO-Ag-Au was found to be −0.50 eV, the E_{VB} value was 1.40 eV [65].

Figure 8 presents a schematic representation of the photocatalytic mechanism based on the band structure calculations. Under light irradiation, e^- in the VB are excited to the CB, leaving behind holes (h^+) that initiate oxidation reactions. The alignment of the CB and VB with the redox potentials of MB facilitates efficient charge transfer, enabling the degradation of organic pollutants. Photogenerated e^-s in Cu_xO nanoparticles is transferred to less negative CB of LrGO-Ag-Au structure. Crucially, photogenerated electrons, especially through highly conductive Ag and Au nanoparticles, reduce adsorbed oxygen molecules and convert them to superoxide anions, because LrGO-Ag-Au's CB potential is more negative than O_2's reduction potential. In this process, electrons in the CB react with dissolved oxygen to form superoxide radicals ($\bullet O_2^-$):

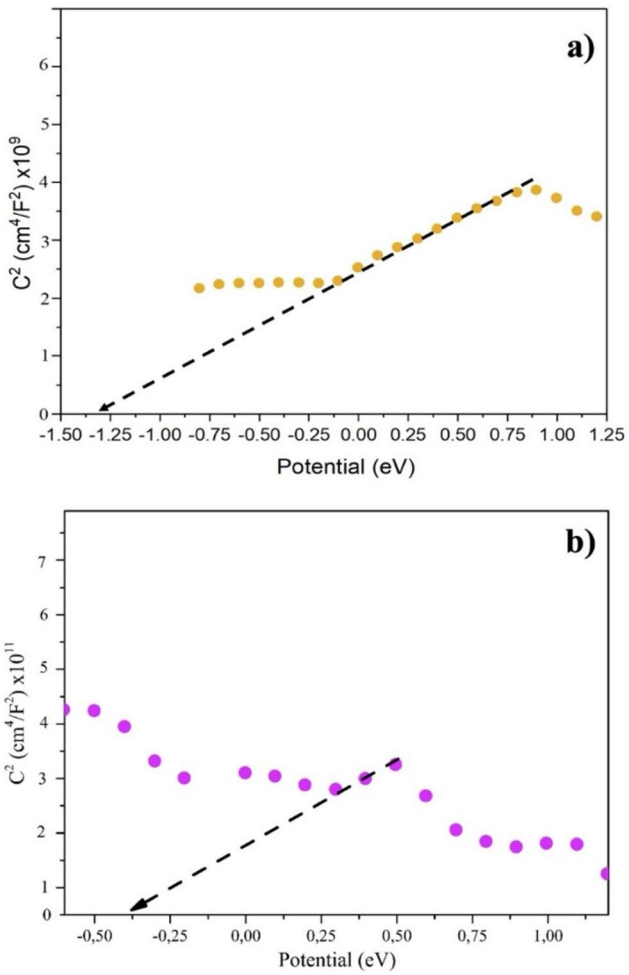


Fig. 7 Mott-Schottky analysis of synthesized nanocomposites: (**a**) Cu_xO, and (**b**) LrGO-Ag-Au

$$O_2 + e^- \rightarrow \cdot O_2^-$$

This reduction process leads to the formation of $O_2^{-}\cdot$ radicals, which can effectively decompose and oxidize organic pollutants. Similarly, photogenerated holes in the VB LrGO-Ag-Au structure are transferred to the lower VB of Cu_xO, since the VB potential of Cu_xO is greater than the oxidation potential of OH^-, hydroxide ions (OH^-) are converted into hydroxyl radicals (-OH), further contributing to the selective degradation process.

In order to gain insight into the dominant reactive species involved in the photocatalytic degradation process, radical scavenging experiments were conducted under identical experimental conditions (Fig. 9). The experiments were performed using benzoquinone (BQ), isopropanol (IPA), and ethylenediaminetetraacetic acid disodium salt (Na_2-EDTA) as scavengers for superoxide radicals ($\bullet O_2^-$), hydroxyl radicals (•OH), and photogenerated holes (h^+), respectively. All experiments were carried out using 3.5 mg of catalyst dispersed in 3.5 mL of 10 ppm MB solution, following a 45-minute dark adsorption–desorption equilibration period prior to illumination. The photocatalytic degradation efficiency after 60 min was measured as 58.6% in the absence of a scavenger. Upon the addition of BQ, the degradation efficiency decreased significantly to 37.3%, indicating a strong suppression of photocatalytic activity. Similarly, the presence of IPA led to a more pronounced decrease to 26.1%, while the addition of Na_2-EDTA resulted in a negligible change (57.8%). These results indicate that •OH radicals and $\bullet O_2^-$ species play a dominant role in the degradation process. In contrast, the limited effect observed with Na_2-EDTA suggests that direct hole oxidation (h^+) plays a comparatively minor role under the present experimental conditions.

Based on the radical trapping results, •OH and $\bullet O_2^-$ species are identified as the dominant reactive species responsible for MB degradation, with •OH playing the primary role. The photocatalyst surface receives the photogenerated electrons (e^-) and holes (h^+). The redox reactions are started by these reactive species ($\bullet O_2^-$, •OH, and h^+), which break down MB. As a result, the breakdown of aromatic rings renders the MB dye solution colorless. The most crucial active species for ring-opening and full MB dye degradation has traditionally been identified as •OH radicals. The first stage of MB degradation is the attack by the •OH on the C–S^+=C functional group. The middle aromatic ring, which contains both heteroatoms S and N, is opened in order to preserve the double bond conjugation that was lost during the transition from C–S^+=C to C–S(=O)–C. The main cause of dye degradation is this kind of complex molecule splitting into smaller, highly oxidized intermediate molecules. During decomposition pathways, •OH radicals target the side chains of MB, resulting in a demethylation reaction. The protonation of the aromatic ring is facilitated by the color shift in MB, which is probably a reversible reaction event. MB dye can also be directly attacked by the VB holes. Owing to the multiphase composition and high electrical conductivity inherent to the LrGO–Ag–Au–Cu_xO hybrid system, the fundamental assumptions underlying Mott–Schottky analysis are not fully satisfied. Consequently, band alignment was determined by integrating the experimentally obtained Mott–Schottky data for Cu_xO with established work function values for Ag, Au, and LrGO reported in the literature. The proposed charge transfer mechanism, illustrated in Fig. 8, aligns with the redox potentials and is indirectly supported by the observed photocatalytic performance of the system.

These findings emphasize the potential of the LrGO–Ag–Au–Cu_xO nanocomposite as an efficient and sustainable photocatalyst for environmental remediation applications. The combination of high degradation efficiency, consistent reaction kinetics, and eco-friendly synthesis positions this

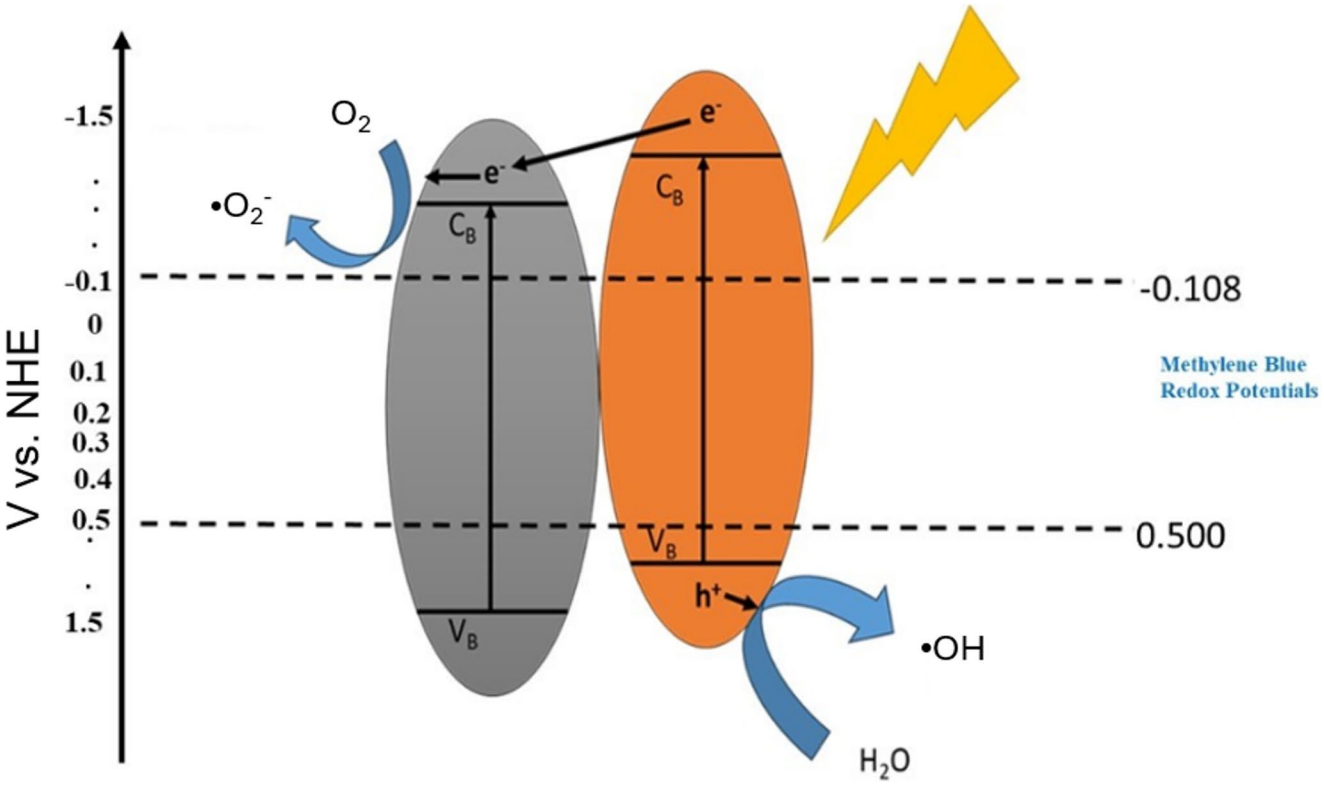


Fig. 8 Photocatalytic mechanism

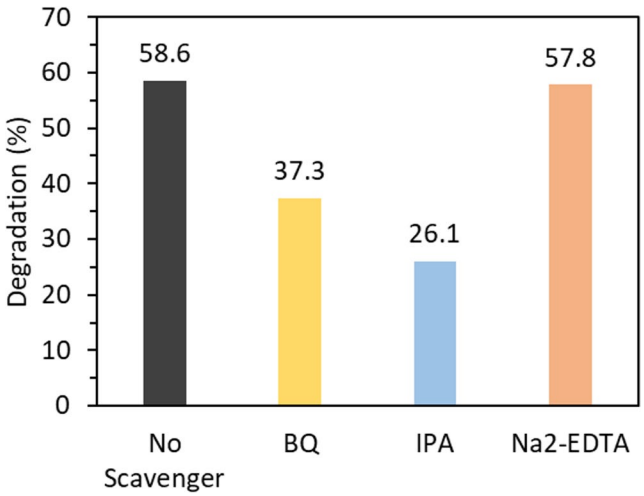


Fig. 9 Effect of different radical scavengers on the photocatalytic degradation of MB over LrGO–Ag–Au–Cu_xO (1:1:1) nanocomposite under visible LED irradiation (experimental conditions: 3.5 mg catalyst, 3.5 mL of 10 ppm MB solution, 45 min dark adsorption-desorption equilibrium, and 60 min irradiation.)

material as a promising candidate for future photocatalytic applications in wastewater treatment and organic pollutant removal.

Conclusion

This study demonstrated that *Cetraria islandica* (L.) Ach. extract can simultaneously reduce graphene oxide and precipitate Ag, Au, and Cu_xO nanoparticles onto the LrGO surface in a single-step process, yielding a well-dispersed quaternary nanocomposite under mild reaction conditions and without the use of toxic organic solvents or noble metal reducing agents. The multiphase composition – comprising metallic Ag and Au alongside CuO/Cu_2O heterojunctions - was independently verified by XRD Rietveld refinement, XPS, and Raman spectroscopy, providing a consistent and complementary characterization picture. The uniform nanoparticle distribution on the LrGO matrix, with an average size of 6.03 ± 2.61 nm, was identified as a key structural feature contributing to the accessible active site density, which outweighs the moderate BET surface area of 11 $m^2 g^{-1}$.

Catalytically, the LrGO–Ag–Au–Cu_xO (1:1:1) nanocomposite reduced 4-NP to 4-AP with an apparent rate constant of 0.0078 ± 0.0003 s^{-1} at 0.172 mg mL^{-1} catalyst loading,

sustaining activity over 11 consecutive cycles. The photocatalytic performance under visible LED irradiation yielded a MB degradation efficiency of 97.67 ± 1.15% within 180 min, with a mean rate constant of 0.0219 ± 0.0027 min^{-1}. Radical scavenging experiments confirmed that •OH and $•O_2^-$ are the primary reactive species, consistent with the proposed charge transfer mechanism involving electron migration from Cu_xO through the LrGO matrix to Ag and Au nanoparticles. The combination of plasmonic enhancement, CuO/Cu_2O heterojunction photocatalysis, and the electron transport capability of LrGO collectively accounts for the observed performance. This work establishes a green, scalable synthesis strategy for quaternary nanocomposites and demonstrates their potential in dual-mode environmental remediation applications.

Supplementary Information The online version contains supplementary material available at https://doi.org/10.1007/s10876-026-03053-8.

Acknowledgements This study was supported by Ankara University Rectorate, Scientific Research Projects Coordination Office (Project No: 21L0443017). The authors gratefully acknowledge Dr. Hakan Eskizengin (Department of Biology, Ankara University) for his assistance with post-catalysis TEM imaging.

Author Contributions Bengü Getiren Sevinç: Conceptualization, Methodology, Investigation, Visualization, Writing – Original Draft. Salih Açıl: Methodology, Investigation, Visualization, Writing – Original Draft. Furkan Soysal: Methodology, Investigation, Writing – Review & Editing. Zafer Çıplak: Methodology, Investigation, Writing – Review & Editing. Atila Yıldız: Writing – Review & Editing. Nuray Yıldız: Supervision, Writing – Review & Editing. All authors reviewed and approved the final version of the manuscript.

Funding Open access funding provided by the Scientific and Technological Research Council of Türkiye (TÜBİTAK).

Data Availability The data that support the findings of this study are available from the corresponding author upon reasonable request.

Declarations

Competing interests The authors declare no competing interests.

Open Access This article is licensed under a Creative Commons Attribution 4.0 International License, which permits use, sharing, adaptation, distribution and reproduction in any medium or format, as long as you give appropriate credit to the original author(s) and the source, provide a link to the Creative Commons licence, and indicate if changes were made. The images or other third party material in this article are included in the article's Creative Commons licence, unless indicated otherwise in a credit line to the material. If material is not included in the article's Creative Commons licence and your intended use is not permitted by statutory regulation or exceeds the permitted use, you will need to obtain permission directly from the copyright holder. To view a copy of this licence, visit http://creativecommons.org/licenses/by/4.0/.

References

1. Abdelfattah A, Ahmed FM, Mohamed LZ, Selim AM (2024) Mechanochemical enhancement in electrode materials via silver-embedded reduced graphene oxide and cobalt oxide nanostructure for supercapacitor applications. Ionics (Kiel) 30:1735–1748. https://doi.org/10.1007/s11581-024-05385-9
2. Abdullah MM, Pal K, Singh P, et al (2024) In-situ growth, and potent photocatalytic performance of gold-decorated reduced graphene oxide (Au/rGO): A soft nanocomposite material. Journal of Molecular Liquids 406:. https://doi.org/10.1016/j.molliq.2024.125096
3. Ahmad A, Siyal AN, Elçi A, Kalwar NH (2024) Ziziphus nummularia leaves extract mediated CuO nanostructures for photocatalytic degradation of Methylene Blue. Desalination and Water Treatment 320:. https://doi.org/10.1016/j.dwt.2024.100667
4. Akbarzadeh E, Soheili HZ, Gholami MR (2019) Novel Cu_2O/Cu-MOF/rGO is reported as highly efficient catalyst for reduction of 4-nitrophenol. Materials Chemistry and Physics 237:. https://doi.org/10.1016/j.matchemphys.2019.121846
5. Ambroz F, Macdonald TJ, Martis V, Parkin IP (2018) Evaluation of the BET theory for the characterization of meso and microporous MOFs. Small Methods 2:. https://doi.org/10.1002/SMTD.201800173
6. Ameta R, Solanki MS, Benjamin S, Ameta SC (2018) Photocatalysis. In: Advanced Oxidation Processes for Wastewater Treatment: Emerging Green Chemical Technology. Elsevier Inc., pp 135–175. https://doi.org/10.1016/B978-0-12-810499-6.00006-1
7. Amirjani A, Amlashi NB, Ahmadiani ZS (2023) Plasmon-Enhanced Photocatalysis Based on Plasmonic Nanoparticles for Energy and Environmental Solutions: A Review. ACS Appl. Nano Mater. 6:9085–9123 https://doi.org/10.1021/acsanm.3c01671
8. Atta D, Wahab HA, Ibrahim MA, Battisha IK (2024) Photocatalytic degradation of methylene blue dye by ZnO nanoparticle thin films, using Sol–gel technique and UV laser irradiation. Sci Rep 14:. https://doi.org/10.1038/s41598-024-76938-1
9. Balık M, Bulut V, Erdogan IY (2019) Optical, structural and phase transition properties of Cu_2O, CuO and Cu_2O/CuO: Their photoelectrochemical sensor applications. Int J Hydrogen Energy 18744–18755. https://doi.org/10.1016/j.ijhydene.2018.08.159
10. Castillo Rodriguez GA (2023)XPS study on determination of binding energy in high purity Ag.. EYA ACADEMY 1:42–53 https://doi.org/10.59335/evur6605
11. Choi J, Oh H, Han SW, et al (2017) Preparation and characterization of graphene oxide supported Cu, Cu_2O, and CuO nanocomposites and their high photocatalytic activity for organic dye molecule. Current Applied Physics 17:137–145. https://doi.org/10.1016/j.cap.2016.11.020
12. Çıplak Z, Getiren B, Gökalp C, et al (2020a) Simultaneous biosynthesis of reduced graphene oxide-Ag-Cu_2O nanostructures by lichen extract for catalytic reduction of textile dyes. Korean Journal of Chemical Engineering 37:2216–2224. https://doi.org/10.1007/s11814-020-0640-0
13. Çıplak Z, Gökalp C, Getiren B, et al (2018) Catalytic performance of Ag, Au and Ag-Au nanoparticles synthesized by lichen extract. Green Processing and Synthesis 7:433–440. https://doi.org/10.1515/gps-2017-0074
14. Çıplak Z, Yıldız A, Yıldız N (2020b) Green preparation of ternary reduced graphene oxide- Au@polyaniline nanocomposite for supercapacitor application. J Energy Storage 32:. https://doi.org/10.1016/j.est.2020.101846
15. Cortés-Santiago A, Vicencio Garrido MA, Pacio M, et al (2026) Validation of the Cançado crystallite size model in rGO–CuO/Cu_2O nanocomposites: Raman-based statistical assessment. Appl Surf Sci 732:. https://doi.org/10.1016/j.apsusc.2026.166568

16. Dardari O, El Idrissi A, El Ouardi M, et al (2024) Polyester fabric supported graphene oxide/Cu-Ag bimetallic nanoparticles as a "dip catalyst" for the reduction of p-nitrophenol and organic dyes. Colloids Surf A Physicochem Eng Asp 697:. https://doi.org/10.1016/j.colsurfa.2024.134314
17. Deng Y, Handoko AD, Du Y, et al (2016) In Situ Raman Spectroscopy of Copper and Copper Oxide Surfaces during Electrochemical Oxygen Evolution Reaction: Identification of CuIII Oxides as Catalytically Active Species. ACS Catal 6:2473–2481. https://doi.org/10.1021/acscatal.6b00205
18. Dhas CR, Malar KCMG, Venkatesh R, et al (2021) Insights on photocatalytic dye inactivation and antimicrobial activity of pH-dependent facile synthesised copper oxide nanoparticles. Appl Phys A Mater Sci Process 127:. https://doi.org/10.1007/s00339-021-05036-0
19. Dixit T, Tripathi A, Solanke S V, et al (2020) Ultra-Wide Bandgap Copper Oxide: High Performance Solar-Blind Photo-detection. IEEE Electron Device Letters 41:1790–1793. https://doi.org/10.1109/LED.2020.3030641
20. Erdem HB, Çetinkaya S (2024) AgNi/PC bimetallic and AgNi/PC@Mn trimetallic nanocatalysts for the efficient reduction of 4-nitrophenol. Catal Commun 187:. https://doi.org/10.1016/j.catcom.2024.106885
21. Fuku X, Modibedi M, Mathe M (2020) Green synthesis of Cu/Cu_2O/CuO nanostructures and the analysis of their electrochemical properties. SN Appl Sci 2:. https://doi.org/10.1007/s42452-020-2704-5
22. Hardiansyah A, Maulana RF, Handayani M, et al (2025) Synthesis and characterization of CuO-ZnO/rGO nanocomposite using one-step hydrothermal method for photodegradation of malachite green (MG) dyes. J Taiwan Inst Chem Eng 106471. https://doi.org/10.1016/j.jtice.2025.106471
23. Hayes OR, Awad Ibrahim A, Samra SE, et al (2023) CuO decorated graphene TiO_2 derived MIL-125 nanocomposite with enhanced photo-response as a highly efficient indirect sunlight driven photocatalyst. J Photochem Photobiol A Chem 442:. https://doi.org/10.1016/j.jphotochem.2023.114800
24. He D, Wang G, Liu G, et al (2017) Construction of leaf-like CuO–Cu_2O nanocomposites on copper foam for high-performance supercapacitors. Dalton Transactions, 46: https://doi.org/10.1039/c7dt00287d
25. Heinemann M, Eifert B, Heiliger C (2013) Band structure and phase stability of the copper oxides Cu_2O, CuO, and Cu_4O_3. Phys Rev B Condens Matter Mater Phys 87:. https://doi.org/10.1103/PhysRevB.87.115111
26. Herzog A, Bergmann A, Jeon HS, et al (2021) Operando Investigation of Ag-Decorated Cu_2O Nanocube Catalysts with Enhanced CO_2 Electroreduction toward Liquid Products. Angew Chem Int Ed 60:7426–7435. https://doi.org/10.1002/anie.202017070
27. Jha K, Raula M, Gomey S, Kalyani C (2025) Recent advances on catalytic potentials of copper oxides (I & II): fundamentals to applications. Critical Reviews in Solid State and Materials Sciences https://doi.org/10.1080/10408436.2025.2560337
28. Jiang L, Wang Y, Feng C (2012) Application of photocatalytic technology in environmental safety. Procedia Engineering 45: 993–997 https://doi.org/10.1016/j.proeng.2012.08.271
29. Kabiri B, Heidari H (2025) Synthesis and catalytic activity of silver- reduced graphene oxide and silver- magnetite- reduced graphene oxide nanocomposites in the reduction of 4-nitrophenol. Sci Rep 15:. https://doi.org/10.1038/s41598-025-98540-9
30. Karuppasamy P, Ramzan Nilofar Nisha N, Pugazhendhi A, et al (2021) An investigation of transition metal doped TiO_2photocatalysts for the enhanced photocatalytic decoloration of methylene blue dye under visible light irradiation. J Environ Chem Eng 9:. https://doi.org/10.1016/j.jece.2021.105254
31. Kaspar TC, Droubay T, Chambers SA, Bagus PS (2010) Spectroscopic evidence for Ag(III) in highly oxidized silver films by X-ray photoelectron spectroscopy. Journal of Physical Chemistry C 114:21562–21571. https://doi.org/10.1021/jp107914e
32. Kassem AA, Abdelhamid HN, Fouad DM, Ibrahim SA (2021) Catalytic reduction of 4-nitrophenol using copper terephthalate frameworks and CuO@C composite. J Environ Chem Eng 9:104401. https://doi.org/10.1016/J.JECE.2020.104401
33. Kayani ZN, Umer M, Riaz S, Naseem S (2015) Characterization of Copper Oxide Nanoparticles Fabricated by the Sol–Gel Method. J Electron Mater 44:3704–3709. https://doi.org/10.1007/s11664-015-3867-5
34. Khan MA, Ullah M, Iqbal T, et al (2015) Assisted Synthesis of Cuprous Oxide (Cu_2O) Nanoparticles via Solvothermal Process. Nanoscience and Nanotechnology Research 3:16–22. https://doi.org/10.12691/nnr-3-1-3
35. Khiavi ND, Katal R, Eshkalak SK, et al (2019) Visible light driven heterojunction photocatalyst of CuO -Cu_2O thin films for photocatalytic degradation of organic pollutants. Nanomaterials 9:. https://doi.org/10.3390/nano9071011
36. Li D, Wu S, Wang Q, et al (2012) Ag@C core-shell colloidal nanoparticles prepared by the hydrothermal route and the low temperature heating-stirring method and their application in surface enhanced Raman scattering. Journal of Physical Chemistry C 116:12283–12294. https://doi.org/10.1021/jp3018088
37. Li X, Kong W, Qin X, et al (2020a) Self-powered cathodic photoelectrochemical aptasensor based on in situ–synthesized CuO-Cu2O nanowire array for detecting prostate-specific antigen. Microchimica Acta 187:. https://doi.org/10.1007/s00604-020-04277-9
38. Li X, Yu J, Jiang C (2020b) Principle and surface science of photocatalysis. Interface Science and Technology. 31:1–38 https://doi.org/10.1016/B978-0-08-102890-2.00001-4
39. Liqiang J, Yichun Q, Baiqi W, et al (2006) Review of photoluminescence performance of nano-sized semiconductor materials and its relationships with photocatalytic activity. Solar Energy Materials and Solar Cells 90:1773–1787. https://doi.org/10.1016/j.solmat.2005.11.007
40. Liu J, Jin J, Deng Z, et al (2012) Tailoring CuO nanostructures for enhanced photocatalytic property. J Colloid Interface Sci 384:1–9. https://doi.org/10.1016/j.jcis.2012.06.044
41. McShane CM, Choi KS (2012) Junction studies on electrochemically fabricated p-n Cu_2O homojunction solar cells for efficiency enhancement. Physical Chemistry Chemical Physics 14:6112–6118. https://doi.org/10.1039/c2cp40502d
42. Mohd Ridzuan ND, Shaharun MS, Din IU, Puspitasari P (2022) Synthesis and Characterization of Nickel–Magnesium Catalyst Supported on Reduced Graphene Oxide. In: Proceedings of the 6th International Conference on Fundamental and Applied Sciences. Springer, Singapore, pp 225–237 https://doi.org/10.1007/978-981-16-4513-6_20
43. Nasrollahzadeh M, Atarod M, Jaleh B, Gandomirouzbahani M (2016) In situ green synthesis of Ag nanoparticles on graphene oxide/TiO_2 nanocomposite and their catalytic activity for the reduction of 4-nitrophenol, congo red and methylene blue. Ceram Int 42:8587–8596. https://doi.org/10.1016/j.ceramint.2016.02.088
44. Nguyen Le My Linh, Dang Thi Thanh Nhan (2024) Kinetics of 4-nitrophenol reduction with $NaBH_4$ over Ag/CuO nanomaterial catalyst. Vietnam Journal of Catalysis and Adsorption 12:153–159. https://doi.org/10.62239/jca.2023.079
45. Nishimura S, Dao ATN, Mott D, et al (2012) X-ray absorption near-edge structure and X-ray photoelectron spectroscopy studies of interfacial charge transfer in gold-silver-Gold double-shell nanoparticles. Journal of Physical Chemistry C 116:4511–4516. https://doi.org/10.1021/jp212031h

46. Patel AR, Fazal AD, Solanky TD, et al (2026) Recent advances and challenges in graphene-based nanomaterials for photocatalytic CO_2reduction. Mater. Adv. 7:109–143 https://doi.org/10.1039/d5ma00750j
47. Ren Z, Li H, Li J, et al (2023) Green synthesis of reduced graphene oxide/chitosan/gold nanoparticles composites and their catalytic activity for reduction of 4-nitrophenol. Int J Biol Macromol 229:732–745. https://doi.org/10.1016/j.ijbiomac.2022.12.282
48. Sarvalkar PD, Jagtap AS, Kalake S V., et al (2024a) Synthesis of Graphene Oxide Anchored Copper Oxide Nanocomposites for Biological Activity and Environmental Remediation. ES Energy and Environment 26:. https://doi.org/10.30919/esee1313
49. Sarvalkar PD, Jamadar AS, kakade SS, et al (2024b) Biogenic synthesis of Co_3O_4 nanoparticles from Aloe barbadensis extract: Antioxidant and antimicrobial activities, and photocatalytic degradation of azo dyes. Results in Engineering 22:. https://doi.org/10.1016/j.rineng.2024.102094
50. Sarvalkar PD, Mandavkar RR, Nimbalkar MS, et al (2021) Biomimetic synthesis of catalytically active nano-silver using Bos taurus (A-2) urine. Sci Rep 11:. https://doi.org/10.1038/s41598-021-96335-2
51. Sing KSW, Everett DH, Haul RAW, et al (2008) Reporting Physisorption Data for Gas/Solid Systems. In: Handbook of Heterogeneous Catalysis. Wiley, pp 1217–1230 https://doi.org/10.1002/9783527610044.hetcat0065
52. Soysal F, Çıplak Z, Gökalp C, et al (2020) One-step hydrothermal synthesis of nitrogen doped reduced graphene oxide-silver nanocomposites: Catalytic performance. Appl Organomet Chem 34:. https://doi.org/10.1002/aoc.5621
53. Swarnkar RK, Singh SC, Gopal R (2009) Synthesis of copper/copper-oxide nanoparticles: Optical and structural characterizations. AIP Conference Proceedings 1147:205–210. https://doi.org/10.1063/1.3183432
54. Sylvestre JP, Poulin S, Kabashin A V., et al (2004) Surface chemistry of gold nanoparticles produced by laser ablation in aqueous media. Journal of Physical Chemistry B 108:16864–16869. https://doi.org/10.1021/jp047134
55. Süzer Ş, Ertaş N, Kumser S, Ataman, OY (1997) X-ray photoelectron spectroscopic characterization of Au collected with atom trapping on silica for atomic absorption spectrometry. Applied spectroscopy 51:1537–1539. https://doi.org/10.1366/0003702971939064
56. Tatarchuk T, Al-Najar B, Bououdina M, Ahmed MAA (2018) Catalytic and Photocatalytic Properties of Oxide Spinels. In: Handbook of Ecomaterials. Springer International Publishing, pp 1–50 https://doi.org/10.1007/978-3-319-48281-1_158-1
57. Thommes M, Kaneko K, Neimark A V., et al (2015) Physisorption of gases, with special reference to the evaluation of surface area and pore size distribution (IUPAC Technical Report). Pure and Applied Chemistry 87:1051–1069. https://doi.org/10.1515/pac-2014-1117
58. Tsuge A, Uwamino Y, Ishizuka T (1990) Determination of Copper(I) and Copper(II) Oxides on a Copper Powder Surface by Diffuse Reflectance Infrared Fourier Transform Spectrometry. Analytical Sciences 6:819–822. https://doi.org/10.2116/analsci.6.819
59. Wang Z, Pischedda V, Saxena SK, Lazor P (2002) X-ray diffraction and Raman spectroscopic study of nanocrystalline CuO under pressures. Solid State Commun 121:275–279. https://doi.org/10.1016/S0038-1098(01)00509-9
60. Wu DY, Zhang M, Zhao LB, Huang YF, Ren B, Tian Z.Q. (2015) Surface plasmon-enhanced photochemical reactions on noble metal nanostructures. Science China Chemistry, 58:574–585. https://doi.org/10.1016/j.jphotochemrev.2013.04.001
61. Wu S, Fu G, Lv W, et al (2018) A Single-Step Hydrothermal Route to 3D Hierarchical Cu_2O/CuO/rGO Nanosheets as High-Performance Anode of Lithium-Ion Batteries. Small 14:. https://doi.org/10.1002/smll.201702667
62. Yang X, He Z, Jin L, et al (2024) Highly Efficient Electrospun Silver Decorated Graphene Oxide Nanocomposites on Poly(vinylidene fluoride) (PVDF@GO-Ag) Hybrid Membrane for Reduction of 4-Nitrophenol. Molecules 29:. https://doi.org/10.3390/molecules29163930
63. Zaleska-Medynska A, Marchelek M, Diak M, Grabowska E (2016) Noble metal-based bimetallic nanoparticles: The effect of the structure on the optical, catalytic and photocatalytic properties. Adv Colloid Interface Sci 229:80–107. https://doi.org/10.1016/j.cis.2015.12.008
64. Zhang Q, Somerville RJ, Chen L, et al (2023) Carbonized wood impregnated with bimetallic nanoparticles as a monolithic continuous-flow microreactor for the reduction of 4-nitrophenol. J Hazard Mater 443:130270. https://doi.org/10.1016/J.JHAZMAT.2022.130270
65. Zhong X, Zhu Y, Sun Q, et al (2022) Tunable Z-scheme and Type II heterojunction of Cu_xO nanoparticles on carbon nitride nanotubes for enhanced visible-light ammonia synthesis. Chemical Engineering Journal 442:. https://doi.org/10.1016/j.cej.2022.136156
66. Ziarati A, Zhao J, Afshani J, et al (2023) Advanced Catalyst for CO_2Photo-Reduction: From Controllable Product Selectivity by Architecture Engineering to Improving Charge Transfer Using Stabilized Au Clusters. Small 19:. https://doi.org/10.1002/smll.202207857

Publisher's Note Springer Nature remains neutral with regard to jurisdictional claims in published maps and institutional affiliations.